A&A 545, A20 (2012)
DOI: 10.1051/0004-6361/201218838

Astronomy & Astrophysics

Searching for heavily obscured post-AGB stars and planetary nebulae

II. Near-IR observations of IRAS sources[⋆]

G. Ramos-Larios[1,⋆⋆,⋆⋆⋆], M. A. Guerrero[1], O. Suárez[2], L. F. Miranda[3,†], and J. F. Gómez[1]

[1] Instituto de Astrofísica de Andalucía (IAA-CSIC), Glorieta de la Astronomía, s/n, 18008 Granada, Spain
e-mail: `[gerardo;mar;jfg]@iaa.es`
[2] Laboratoire Lagrange, UMR 7293, Université de Nice Sophia-Antipolis, CNRS, Observatoire de la Côte d'Azur, 06300 Nice, France
e-mail: `olga.suarez@unice.fr`
[3] Consejo Superior de Investigaciones Científicas (CSIC), c/ Serrano 117, 28006 Madrid, Spain
e-mail: `lfm@iaa.es`

Received 18 January 2012 / Accepted 19 June 2012

ABSTRACT

The most massive AGB stars are expected to result in heavily obscured post-AGB stars, proto-PNe and PNe with highly axisymmetric morphologies. To investigate this evolutionary connection, we have selected a sample of 165 presumably obscured IRAS post-AGB star and PN candidates and obtained near-IR *JHK* images for 164 of them. These images, in conjunction with DSS, 2MASS, *Spitzer* GLIMPSE, MSX, AKARI, and IRAS archival data, have allowed us to identify the near-IR counterparts of 154 of these sources, providing reliable finding charts and coordinates. Near-IR narrow-band Brγ, H$_2$, and K continuum images were acquired for 6 of these sources that were found to be resolved in near-IR *JHK* images. Among the extended post-AGB source and PN candidates, three are round and seven have bipolar morphologies. Five of the extended sources are ionized and may have thus entered the PN stage. We note that all extended sources with water maser emission have bipolar morphology. We have investigated the Galactic distribution of sources with the largest flux drop from the 9 μm AKARI band to the near-IR J band and found that the width of the distribution in Galactic latitude is consistent with those of bipolar PNe and DUPLEX (DUst-Prominent Longitudinally EXtended) sources.

Key words. stars: AGB and post-AGB – stars: evolution – planetary nebulae: general

1. Introduction

Stars between 1 and 8 $M_\odot$, after having exhausted the nuclear combustible at their cores, ascend the asymptotic giant branch (AGB), where they suffer heavy mass loss episodes with mass-loss rates up to several times 10^{-4} $M_\odot$ yr $^{-1}$ (e.g., Hoogzaad et al. 2002). The envelope expelled during this evolutionary stage will usually obscure the central star at optical wavelengths, and strong IR radiation is emitted instead (Pottasch et al. 1988). When the mass loss that characterizes the AGB ceases and the star enters the post-AGB phase (see Soker 2008, for a precise quantitative definition of this moment), the circumstellar envelope ejected in the AGB phase expands and cools while the effective temperature of the central star increases progressively (Blöcker 1995b). At the time the central star becomes hot enough to ionize the circumstellar envelope ($T_{\rm eff} \geq 25\,000$ K), a planetary nebula (PN) arises.

The circumstellar envelope of an AGB star can be optically thick during its late AGB evolution, but its subsequent expansion during the post-AGB phase will make the star visible again at optical wavelengths. The exact time and the temperature of the star when this occurs are governed by the mass-loss rate during the AGB (and thus the optical thickness of the envelope) which is ultimately related to the stellar mass (Schönberner 1981; Vassiliadis & Wood 1993; Blöcker 1995a). The most massive stars will even traverse the whole post-AGB phase being invisible at optical wavelengths, and may reach the PN phase while still not detectable in the visible domain (e.g., IRAS 17347−3139, de Gregorio-Monsalvo et al. 2004). These optically obscured sources that may represent the most massive stars in these evolutionary phases are obviously of great interest.

Objects in the transition from the AGB to the PN phase have strong far-infrared (far-IR) excess and the use of IRAS data has generated extensive catalogues of post-AGB and young PN candidates (e.g., Pottasch et al. 1988). The identification and characterization of post-AGB sources have been so far hampered by the limited astrometric accuracy of the IRAS sources, ∼15″–30″. This task is particularly difficult in the case of heavily obscured sources that cannot be detected in the optical (Suárez et al. 2006). Near-IR JHK observations can be well suited for the

---

[⋆] Based on observations collected at the European Organization for Astronomical Research in the Southern Hemisphere, Chile (081.D-0812), observations made with the Italian Telescopio Nazionale Galileo (TNG) operated on the island of La Palma by the Fundación Galileo Galilei of the INAF (Istituto Nazionale di Astrofisica) at the Spanish Observatorio del Roque de los Muchachos of the Instituto de Astrofísica de Canarias, and on observations with AKARI, a JAXA project with the participation of ESA.

[⋆⋆] Postdoctoral Research Fellow.

[⋆⋆⋆] *Current address*: Instituto de Astronomía y Meteorología, Av. Vallarta No. 2602, Col. Arcos Vallarta, 44130 Guadalajara, Jalisco, Mexico; e-mail: `gerardo@astro.iam.udg.mx`

[†] *Present address*: Departamento de Física Aplicada, Facultade de Ciencias, Campus Lagos-Marcosende s/n, Universidade de Vigo, 36310 Vigo, Spain.

Table 1. Technical characteristics of the near-IR filters.

Band	TNG NICS			NTT SOFI		
	λ_c (μm)	*FWHM* (μm)	Peak transmission (%)	λ_c (μm)	*FWHM* (μm)	Peak transmission (%)
J	1.27	0.30	78	1.247	0.290	90
H	1.63	0.30	86	1.653	0.297	83
K	2.12	0.35	94	2.162	0.275	88
H_2	2.122	0.032	70	2.124	0.028	78
Brγ	2.169	0.035	72	2.167	0.028	71
K-continuum	2.275	0.039	68	2.280	0.030	69

accurate identification of IRAS post-AGB candidates. A significant effort has been carried out by Manchado et al. (1989), García-Lario et al. (1990) and García-Lario et al. (1997), who obtained JHK photometric observations of a large sample of post-AGB candidates.

The examination of more recent 2MASS data has shown that the use of single-element photometers may not be adequate for the identification of optically obscured sources (e.g., Jiménez-Esteban et al. 2006b; Szczerba et al. 2007), resulting in the misidentification of sources in crowded fields. We have further developed this technique (Ramos-Larios et al. 2009, hereafter Paper I) to search for near-IR counterparts in the 2MASS Point Source Catalog (PSC) of heavily obscured post-AGB stars, proto-PNe and PNe among a sample of 165 IRAS sources that, fulfilling the selection criteria of post-AGB candidates described by Suárez et al. (2006), show strong indications of being invisible at optical wavelengths.

The near-IR identification and characterization of ~85 of the IRAS sources in our sample was not possible in Paper I because 2MASS has a limited sensitivity (its detection limit is $J = 15.8$ mag, $H = 15.1$ mag, and $K = 14.3$ mag). Therefore, the results presented in Paper I were biased towards the less obscured objects in our sample. Furthermore, Paper I purposely excluded resolved objects because the morphological information from 2MASS images, at a spatial resolution ~2″, was poor and their near-IR photometry was uncertain. These sources, however, may be key objects in the transition from the AGB to the PN phases.

To complete the results of Paper I and to search for circumstellar shells at a greater spatial resolution, ~1″, we have obtained near-IR JHK imaging observations of the IRAS sources in our sample. The improved sensitivity and spatial resolution of the new near-IR data, in conjunction with the improved coordinates provided by AKARI, have allowed us to identify near-IR counterparts for most of the sources in Paper I that could not be detected or resolved from nearby sources in 2MASS images. The photometric measurements of the new JHK images have been used to derive the spectral energy distributions (SED) in the IR domain of the sources with newly identified near-IR counterparts, and to search for near-IR variability among the sources with 2MASS PSC counterparts studied in Paper I. Finally, the morphology of the objects in our sample that are found to be extended is also presented.

The new near-IR observations and archival MSX, *Spitzer* GLIMPSE, and AKARI data are described in Sect. 2. The new information obtained for the objects with 2MASS PSC counterpart studied in Paper I is given in Sect. 3, while the identification of new near-IR counterparts and the morphology of extended sources are described in Sects. 4 and 5, respectively. Finally, we discuss the results in Sect. 6 and provide a summary of the main findings in Sect. 7.

2. Observations

2.1. Near-IR observations

2.1.1. Data acquisition

Near-IR JHK images of the objects in our sample (see Table 1 in Paper I) have been obtained using the 3.58 m Telescopio Nazionale Galileo (TNG) at the Observatorio del Roque de los Muchachos (La Palma, Spain) and the 3.6 m New Technology Telescope (NTT) at La Silla Observatory (Chile). Northern objects ($\delta > -5°$) were observed at the TNG during three observing runs on June, August, and October 2008, while Southern objects ($\delta < -5°$) were observed at the NTT on July 2008. Only IRAS 08242−3828 has not been observed because this Southern source was not visible during the NTT observing run on July 2008.

The Near Infrared Camera Spectrometer (NICS), a multimode instrument for IR observations in the range 0.9–2.5 μm (Baffa et al. 2001), was used at the TNG. NICS employs a Rockwell 1024×1024 HgCdTe Hawaii array. The large field (LF) mode was used, providing a plate scale of 0.″25 pixel^{-1} and a field of view of 4.′2 × 4.′2. At the NTT, the Son OF Isaac (SOFI) near-IR spectrograph and camera (Moorwood et al. 1998) was used. SOFI is equipped with a similar Rockwell 1024 × 1024 HgCdTe Hawaii array, providing a pixel scale of 0.″288 pixel and a field of view of 4.′92 × 4.′92 in its large field (LF) mode. The observations were carried out under photometric conditions and the seeing for most of the observations was 0.″7–0.″8 at the TNG and 0.″8–1.″2 at the NTT.

Broad-band JHK images were obtained at both telescopes. We note that the characteristics of the filters used at each telescope are not exactly the same; their central wavelengths, bandwidths, and transmission peaks are listed in Table 1. The most remarkable difference among the filters used in the observations occurs in the K band. The K short (K_s) filter used at SOFI is notably different from both the K' filter used at NICS (Wainscoat & Cowie 1992) and the standard K filter; the red edge of the K_s filter is similar to that of the K' filter, but its blue edge is more alike that of the standard K filter. This special design allows the K_s filter to avoid both the atmospheric absorption feature at 1.9 μm and the thermal background radiation beyond 2.3 μm. In our work, we will convert both K_s and K' magnitudes into standard K magnitudes using the expressions:

$$K - K_s = -0.005\,(J - K), \tag{1}$$

$$K' - K = 0.19\,(H - K) \tag{2}$$

provided by the SOFI User's Manual (ESO Doc. No. LSO-MAN-ESO-40100-0004) and Wainscoat & Cowie (1992), respectively.

These near-IR observations consisted of series of several integrations repeated at dithered positions on the detector. As for

Table 2. Extended sources observed in H_2, Brγ, and K-continuum.

IRAS name	Telescope	Instrument	$t_{\rm int}$ (s)	Number of integrations	Number of images	$t_{\rm exp}$ (s)	Seeing ($''$)
12405−6219	NTT	SOFI	45	5	7	1575	1.5
15103−5754	NTT	SOFI	45	5	7	1575	1.0
15452−5459	NTT	SOFI	5	5	11	275	0.8
15534−5422	NTT	SOFI	45	5	7	1575	1.5
16333−4807	NTT	SOFI	35	5	7	1225	1.2
19071+0857	NTT	SOFI	45	5	7	1575	1.2
	TNG	NICS	30	5	7	1050	0.6

the TNG NICS observations of Northern sources, 5–10 integrations of exposure time 3 to 10 s, depending on the brightness of the object, were taken at 5–7 different CCD locations for each object and filter. Therefore, total effective exposures ranging between 75 and 500 s were secured. Since the shortest exposure time of an individual frame allowed by the control software was 3 s, a grey attenuator filter was used to reduce the count rate of the brightest objects (e.g., IRAS 20406+2953) and to avoid the saturation of the signal. This filter reduced the brightness of the object by 5.1 mag, 5.5 mag, and 5.7 mag in the J, H, and K bands, respectively, but its use has the drawback of limiting the accuracy of the photometric measurements to ~0.2 mag. Likewise, the NTT SOFI observations of Southern sources consisted of 5 integrations of exposure time from 1.2 to 8 s at 7 positions on the CCD randomly determined by the img_obs_Jitter template. The total effective exposure, resulting from the co-addition of the 35 short jittered exposures, ranged from 42 to 280 s.

Six of the objects that were found to present extended emission in JHK images (Table 2) were also observed using the H_2, Brγ, and K-continuum narrow-band filters whose characteristics are listed in Table 1. The observations consisted of a number of jittered images, each one being the average of five integrations. For each object, the integration time of each individual frame, the number of integrations and images, and the total exposure time are listed in Table 2. The spatial resolution of the images, as determined from the FWHM of stars in the field of view, is also listed in the last column of Table 2.

2.1.2. Data reduction, calibration and analysis

The standard reduction of near-IR data includes the dark subtraction and flat field correction of individual frames that are then median combined to build a sky image. The sky image is subsequently subtracted from the individual frames that are then shifted and finally stacked into one single image. As for the TNG NICS JHK' data, their reduction was mostly carried out using SNAP (Speedy Near-IR data Automatic reduction Pipeline), a pipeline for the automatic reduction of near-IR data that uses software routines of IRDR[1], IRAF[2], Sextractor, and Drizzle[3]. The reduction performed by SNAP includes additional non-standard steps such as cross-talk correction, double-pass sky subtraction, and field distortion correction[4]. When SNAP was not used, the standard reduction was performed using standard routines within IRAF, but an additional cross-talk correction was carried out at the beginning of the reduction process. The reduction of the NTT SOFI $JHK_{\rm s}$ data was performed using the SOFI pipeline sofi_img_jitter which is part of the SOFI subsystem of the VLT data flow system (DFS). The sofi_img_jitter tool carries out the standard near-IR reduction, including additional steps for cross-talk effect correction and bad pixels cleaning as described in the SOFI pipeline user manual (VLT-MAN-ESO-19500-4284).

At least three different photometric standard stars were observed each night for photometric calibrations. At the TNG, we observed the standard stars AS5, AS17, AS29, AS31, AS33, and AS36 (Hunt et al. 1998). The effective exposure time for these stars varies from 75 s up to 175 s, consisting of 5–7 dithered images, each one being the average of 5 frames with integration times between 3 and 7 s. At the NTT, we observed the infrared NICMOS standard stars #9103, #9146, #9157, #9185, #9186, and #9187 (Persson et al. 1998). The effective exposure time for these stars is 50 s, consisting of 5 jittered images, each one being the average of five 2-s integrations.

Using routines of the IRAF *daophot* package, aperture photometry was performed to derive the JHK magnitudes listed in Tables 3–6. The tables include references to previous works reporting JHK measurements. For point sources, different aperture sizes and sky annuli were used depending on the PSF of the source. Photometric instrumental zero-points for the TNG standard stars were calculated using this method, while, for the NTT standard stars, the zero-point tool of Gasgano (a data file organizer developed and maintained by the European Southern Observatory, ESO) was used. For extended sources (e.g., IRAS 15452−5459), we used the HEASARC task *fv* (the interactive FITS file editor) to determine their background-subtracted fluxes and uncertainties by comparing the count numbers and deviations of source regions encompassing the extended emission with those of appropriate nearby background regions. The 1-σ error-bars of the JHK magnitudes provided in Tables 3–6 include systematic uncertainties of the calibration, aperture and sky annuli selection, and PSF estimate, as well as the photon noise. The limiting magnitudes at the NTT were found to be J = 22.7 mag, H = 21.8 mag, and K = 20.4 mag,

---

[1] IRDR, the Infra-Red Data Reduction, is a C library and set of standalone C programs and perl scripts for processing IR imaging data that is distributed by the Institute of Astronomy (IoA), at the University of Cambridge.

[2] IRAF, the Image Reduction and Analysis Facility, is distributed by the National Optical Astronomy Observatory, which is operated by the Association of Universities for Research in Astronomy (AURA) under cooperative agreement with the National Science Foundation.

[3] Drizzle is available as an IRAF task as part of the Space Telescope Science Data Analysis System (STSDAS) package and can be retrieved from the Space Telescope Science Institute (STScI) web site.

[4] Full details of these non-standard reduction steps are provided at `http://www.arcetri.astro.it/~filippo/snap`

Table 3. NTT/TNG *JHK* magnitudes of IRAS post-AGB star and PN candidates with counterparts in the 2MASS PSC.

IRAS name	*J* (mag)	*H* (mag)	*K* (mag)	Ref.
00509+6623	13.701 ± 0.010	12.188 ± 0.008	10.707 ± 0.014	
09055−4629	15.91 ± 0.04	14.34 ± 0.04	11.919 ± 0.028	
09102−5101	14.17 ± 0.04	13.69 ± 0.04	12.608 ± 0.028	
09119−5150	14.17 ± 0.04	13.24 ± 0.04	11.74 ± 0.03	4
09378−5117	12.22 ± 0.04	10.92 ± 0.04	10.29 ± 0.03	
09500−5236	18.03 ± 0.08	15.41 ± 0.04	12.33 ± 0.03	
11339−6004	15.60 ± 0.04	14.49 ± 0.04	13.70 ± 0.03	4, 6
11488−6432	10.62 ± 0.04	9.20 ± 0.03	8.28 ± 0.03	
12262−6417	12.67 ± 0.04	10.99 ± 0.03	9.37 ± 0.03	6
12309−5928	16.15 ± 0.07	13.90 ± 0.06	11.88 ± 0.06	6
13398−5951	13.47 ± 0.07	12.00 ± 0.06	10.80 ± 0.06	
13421−6125	12.13 ± 0.04	10.97 ± 0.04	10.46 ± 0.03	4, 6
13483−5905	13.61 ± 0.07	12.64 ± 0.06	12.29 ± 0.06	
14104−5819	19.98 ± 0.25	15.31 ± 0.05	12.049 ± 0.028	4, 6
14521−5300	11.07 ± 0.04	10.32 ± 0.04	9.898 ± 0.027	
15038−5533	15.02 ± 0.04	13.01 ± 0.04	11.84 ± 0.03	
15408−5657	20.31 ± 0.17	14.18 ± 0.04	10.411 ± 0.026	4
16279−8158	10.90 ± 0.05	9.93 ± 0.04	9.352 ± 0.024	
16517−3626	13.39 ± 0.05	12.13 ± 0.06	11.85 ± 0.06	
16559−2957	11.65 ± 0.04	10.77 ± 0.04	9.346 ± 0.026	3, 6
16567−3838	>22.7	19.73 ± 0.12	14.619 ± 0.026	
16584−3710	17.55 ± 0.07	14.08 ± 0.03	11.64 ± 0.03	
17010−3810	13.30 ± 0.04	12.91 ± 0.04	11.703 ± 0.026	
17021−3109	18.09 ± 0.10	16.28 ± 0.05	13.88 ± 0.03	
17021−3054	14.77 ± 0.04	13.22 ± 0.04	11.785 ± 0.026	4
17149−3053	17.56 ± 0.09	15.59 ± 0.05	13.42 ± 0.03	4, 6
17175−2819	12.51 ± 0.04	11.52 ± 0.04	10.759 ± 0.026	
17233−2602	15.21 ± 0.04	14.13 ± 0.04	12.916 ± 0.028	
17291−2147	13.49 ± 0.04	12.25 ± 0.04	11.081 ± 0.026	
17359−2902	12.74 ± 0.04	11.31 ± 0.04	10.439 ± 0.026	
17385−3332	10.46 ± 0.04	9.54 ± 0.04	9.075 ± 0.026	6
17499−3520	10.61 ± 0.04	10.01 ± 0.04	9.777 ± 0.023	
17540−2753	12.42 ± 0.04	11.00 ± 0.04	10.106 ± 0.026	4
17548−2753	14.79 ± 0.05	12.73 ± 0.04	11.431 ± 0.027	
17550−2800	13.92 ± 0.07	11.50 ± 0.06	9.39 ± 0.06	4, 6
17580−3111	11.04 ± 0.05	10.24 ± 0.04	9.035 ± 0.021	6
17582−2619	14.95 ± 0.04	12.64 ± 0.04	11.097 ± 0.028	4
17596−3952	9.59 ± 0.04	8.78 ± 0.04	8.341 ± 0.027	
18015−1352	20.06 ± 0.10	18.68 ± 0.07	14.945 ± 0.027	
18049−2118	>22.7	16.35 ± 0.04	11.122 ± 0.028	
18071−1727	17.08 ± 0.04	14.63 ± 0.04	12.648 ± 0.024	2, 6
18105−1935	13.07 ± 0.05	10.88 ± 0.04	9.741 ± 0.025	
18183−2538	14.89 ± 0.05	13.29 ± 0.04	10.70 ± 0.03	
18199−1442	>22.7	17.00 ± 0.05	10.997 ± 0.024	
18229−1127	12.58 ± 0.04	11.40 ± 0.03	10.69 ± 0.03	4
18236−0447	18.23 ± 0.06	15.37 ± 0.04	13.06 ± 0.03	4
18355−0712	15.87 ± 0.07	13.13 ± 0.04	11.52 ± 0.03	
18361−1203	11.76 ± 0.05	10.64 ± 0.03	10.044 ± 0.026	
18434−0042	16.316 ± 0.021	14.149 ± 0.017	12.807 ± 0.017	
18454+0001	14.432 ± 0.014	13.248 ± 0.010	12.506 ± 0.014	4, 6
18470+0015	14.062 ± 0.016	12.462 ± 0.011	10.767 ± 0.014	
18485+0642	13.906 ± 0.015	12.867 ± 0.011	12.321 ± 0.014	4, 6
18524+0544	14.567 ± 0.015	13.692 ± 0.011	12.403 ± 0.014	
18576+0341	12.544 ± 0.010	9.73 ± 0.20	7.79 ± 0.20	5
19006+1022	15.829 ± 0.021	13.499 ± 0.009	11.212 ± 0.014	
19075+0432	10.847 ± 0.010	10.06 ± 0.20	8.44 ± 0.20	3, 6
19079−0315	11.98 ± 0.05	11.20 ± 0.04	10.528 ± 0.024	
19083+0119	16.86 ± 0.03	15.522 ± 0.020	14.332 ± 0.015	
19094+1627	12.783 ± 0.010	11.716 ± 0.010	11.081 ± 0.012	
19134+2131	16.281 ± 0.024	14.554 ± 0.012	13.122 ± 0.012	6
19176+1251	15.916 ± 0.017	14.513 ± 0.012	13.023 ± 0.014	4, 6
19181+1806	13.413 ± 0.011	12.007 ± 0.008	10.901 ± 0.014	6
19193+1804	17.51 ± 0.03	15.563 ± 0.013	14.262 ± 0.013	4
19319+2214	13.385 ± 0.010	11.831 ± 0.008	10.581 ± 0.014	
19374+2359	11.791 ± 0.010	10.747 ± 0.008	9.768 ± 0.014	2, 6
20174+3222	10.884 ± 0.010	10.26 ± 0.20	9.71 ± 0.20	1, 6
20214+3749	16.90 ± 0.03	14.026 ± 0.012	11.253 ± 0.014	
20244+3509	9.492 ± 0.014	8.812 ± 0.010	7.644 ± 0.20	4, 6
20406+2953	10.79 ± 0.20	8.9 ± 0.4	7.9 ± 0.7	4
20461+3853	11.362 ± 0.010	10.53 ± 0.20	9.82 ± 0.20	4, 6
21525+5643	18.109 ± 0.016	14.674 ± 0.011	12.193 ± 0.014	6

References. References to previous *JHK* measurementes. (1) Manchado et al. (1989), (2) Van der Veen et al. (1989), (3) García-Lario et al. (1990), (4) García-Lario et al. (1997), (5) Jiménez-Esteban et al. (2006a), (6) Szczerba et al. (2007).

Table 4. Sources with differing NTT/TNG and 2MASS PSC *JHK* magnitudes.

IRAS name	2MASS			NTT or TNG					
	J (mag)	*H* (mag)	*K* (mag)	*J* (mag)	*H* (mag)	*K* (mag)	Δ*J* (mag)	Δ*H* (mag)	Δ*K* (mag)
09500−5236	>15.8	14.62 ± 0.06	11.845 ± 0.023	18.03 ± 0.08	15.41 ± 0.04	12.33 ± 0.03	. . .	0.79 ± 0.07	0.48 ± 0.04
14104−5819	>15.8	14.20 ± 0.09	10.690 ± 0.024	19.98 ± 0.25	15.31 ± 0.05	12.049 ± 0.028	. . .	1.10 ± 0.10	1.36 ± 0.04
15408−5657	>15.8	>15.1	11.519 ± 0.026	20.31 ± 0.17	14.18 ± 0.04	10.411 ± 0.026	. . .	. . .	–1.11 ± 0.04
16279−8158	10.308 ± 0.023	9.263 ± 0.025	8.818 ± 0.023	10.90 ± 0.05	9.93 ± 0.04	9.352 ± 0.024	0.59 ± 0.06	0.67 ± 0.05	0.53 ± 0.03
16517−3626	12.652 ± 0.026	11.900 ± 0.025	11.2:	13.39 ± 0.05	12.13 ± 0.06	11.85 ± 0.06	0.74 ± 0.06	0.23 ± 0.07	0.7:
17010−3810	13.110 ± 0.022	12.040 ± 0.028	11.302 ± 0.020	13.30 ± 0.04	12.91 ± 0.04	11.703 ± 0.026	0.19 ± 0.05	0.87 ± 0.05	0.40 ± 0.03
17550−2800	12.5:	11.04 ± 0.06	8.9:	13.92 ± 0.07	11.50 ± 0.06	9.39 ± 0.06	1.4:	0.46 ± 0.08	0.5:
17580−3111	12.402 ± 0.024	10.551 ± 0.022	9.280 ± 0.019	11.04 ± 0.05	10.24 ± 0.04	9.035 ± 0.021	–1.36 ± 0.06	–0.31 ± 0.05	–0.25 ± 0.03
18071−1727	>15.8	14.1:	12.71 ± 0.06	17.08 ± 0.04	14.63 ± 0.04	12.648 ± 0.024	. . .	0.5:	–0.07 ± 0.07
18105−1935	11.3:	10.81 ± 0.04	9.2:	13.07 ± 0.05	10.88 ± 0.04	9.741 ± 0.025	1.7:	0.07 ± 0.06	0.5:
18183−2538	14.59 ± 0.04	13.043 ± 0.026	11.344 ± 0.023	14.89 ± 0.05	13.29 ± 0.04	10.70 ± 0.03	0.30 ± 0.06	0.25 ± 0.05	–0.64 ± 0.04
18576+0341	12.164 ± 0.027	8.918 ± 0.028	7.007 ± 0.020	12.544 ± 0.010	9.73 ± 0.20	7.79 ± 0.20	0.38 ± 0.03	0.81 ± 0.20	0.78 ± 0.20
21525+5643	>15.8	>15.1	13.50 ± 0.07	18.109 ± 0.016	14.674 ± 0.011	12.193 ± 0.014	. . .	. . .	–1.31 ± 0.07

Notes. Magnitudes marked by ":" are uncertain.

while at the TNG these were found to be $J = 22.5$ mag, $H = 21.4$ mag, and $K = 20.2$ mag We note that the NTT SOFI JHK_s images of objects brighter than $J > 9$ mag and $K > 7$ mag saturated using the shortest integration time (1.2 s) that SOFI control software could afford. Consequently, we do not present new *JHK* magnitudes for these objects, all of them having a 2MASS PSC counterpart. Their images were nonetheless acquired and examined in order to search for extended emission.

Table 5. Near-IR properties of IRAS post-AGB star and PN candidates.

IRAS name	α (J2000)	δ (J2000)	Spatial properties	DSS	2MASS	J (mag)	H (mag)	K (mag)	Ref.
04137+7016	04 19 08.43	+70 23 26.4	PS	Y	Y	12.499 ± 0.010	10.577 ± 0.008	11.185 ± 0.014	
05573+3156	06 00 33.38	+31 56 44.2	E	N	Y	14.421 ± 0.015	11.844 ± 0.014	9.703 ± 0.018	4
06499+0145	06 52 28.23	+01 42 05.8	E	Y	Y	16.124 ± 0.017	15.012 ± 0.014	14.001 ± 0.019	4
08351−4634	08 36 45.65	−46 44 44.8	PS	N	N	>22.7	21.42 ± 0.16	17.88 ± 0.07	4, 6
10194−5625	10 21 15.15	−56 40 32.4	PS	N	N	>22.7	21.46 ± 0.16	17.44 ± 0.06	6
11381−6401	11 40 31.86	−64 18 28.1	PS	Y	Y	15.05 ± 0.04	14.00 ± 0.04	13.351 ± 0.028	6
11444−6150	11 46 54.59	−62 07 11.2	PS	N	N	18.20 ± 0.10	16.26 ± 0.06	14.80 ± 0.04	4
11549−6225	11 57 30.46	−62 42 11.2	PS	N	N	>22.7	>21.8	16.11 ± 0.05	
12360−5740	12 38 53.11	−57 56 31.7	PS	Y	Y	10.33 ± 0.03	10.04 ± 0.03	9.84 ± 0.03	4, 6
12405−6219	12 43 31.50	−62 36 14.0	PS	N	Y	16.75 ± 0.08	14.03 ± 0.08	10.79 ± 0.07	
13293−6000	13 32 39.21	−60 15 39.1	PS	N	Y	18.35 ± 0.13	15.11 ± 0.05	12.32 ± 0.03	
13404−6059	13 43 50.40	−61 14 31.0	E?	N	N	20.09 ± 0.20	18.21 ± 0.08	17.82 ± 0.09	
13427−6531	13 46 25.70	−65 46 24.2	PS	Y	Y	14.02 ± 0.04	13.53 ± 0.03	12.953 ± 0.025	4
13500−6106	13 53 34.29	−61 20 51.2	E?	N	N	19.48 ± 0.15	17.44 ± 0.07	16.32 ± 0.05	4
13529−5934	13 56 24.61	−59 48 57.3	PS	Y	Y	14.262 ± 0.04	13.15 ± 0.04	12.23 ± 0.03	6
14249−5310	14 28 24.84	−53 24 04.5	PS	N	Y	11.79 ± 0.05	9.32 ± 0.04	7.93 ± 0.03	
15103−5754	15 14 18.45	−58 05 20.3	E	N	Y	15.17 ± 0.04	12.37 ± 0.03	10.29 ± 0.03	4
15229−5433	15 26 40.57	−54 44 17.1	PS	Y	Y	14.71 ± 0.06	13.95 ± 0.05	13.11 ± 0.04	
15284−6026	15 32 37.03	−60 37 04.8	PS	N	N	>22.7	19.03 ± 0.12	16.49 ± 0.04	
15452−5459	15 49 11.34	−55 08 51.7	E	N	Y	9.79 ± 0.05	7.89 ± 0.04	6.76 ± 0.06	6
15531−5704	15 57 10.51	−57 13 18.0	PS	N	N	20.63 ± 0.07	20.77 ± 0.07	20.01 ± 0.06	
15534−5422	15 57 21.11	−54 30 46.4	E	Y	Y	13.75 ± 0.04	12.94 ± 0.04	11.728 ± 0.025	
16209−4714	16 24 34.01	−47 21 30.5	PS	Y	Y	12.16 ± 0.05	10.83 ± 0.03	10.01 ± 0.03	
16245−3859	16 27 53.10	−39 05 44.7	PS	N	N	>22.7	18.46 ± 0.08	16.17 ± 0.04	
16296−4507	16 33 12.53	−45 13 43.8	PS	Y	Y	14.78 ± 0.07	13.46 ± 0.06	13.14 ± 0.06	
16333−4807	16 37 06.63	−48 13 42.5	E	N	Y	15.07 ± 0.04	13.39 ± 0.03	11.242 ± 0.024	
16507−4810	16 54 31.04	−48 15 22.5	PS	Y	Y	11.33 ± 0.04	10.39 ± 0.04	9.829 ± 0.026	
16518−3425	16 55 06.11	−34 30 06.4	PS	N	N	20.88 ± 0.15	19.56 ± 0.13	18.37 ± 0.12	
17009−4154	17 04 29.63	−41 58 38.9	E	N	Y	12.53 ± 0.04	10.37 ± 0.03	8.89 ± 0.03	4, 6
17052−3245	17 08 33.20	−32 49 45.0	PS	N	Y	19.11 ± 0.14	17.04 ± 0.06	14.95 ± 0.04	
17067−3759	17 10 08.61	−38 03 21.4	PS	N	N	16.70 ± 0.05	15.73 ± 0.05	14.50 ± 0.04	4, 6
17097−3624	17 03 05.30	−36 27 52.4	PS	N	N	>22.7	20.79 ± 0.15	17.89 ± 0.06	
17150−3224	17 18 19.85	−32 27 21.6	E	Y	Y	10.76 ± 0.04	9.95 ± 0.03	9.261 ± 0.024	4, 6
17158−4049	17 19 19.66	−40 52 40.5	PS	N	N	16.93 ± 0.05	15.71 ± 0.04	14.79 ± 0.03	
17168−3736	17 20 15.07	−37 39 34.4	PS	N	N	>22.7	19.02 ± 0.18	15.04 ± 0.05	4
17234−4008	17 26 56.11	−40 11 03.1	PS	N	Y	16.16 ± 0.05	14.54 ± 0.05	12.90 ± 0.03	4, 6
17269−2235	17 29 58.25	−22 37 34.2	PS	Y	Y	11.97 ± 0.03	10.50 ± 0.03	9.79 ± 0.03	4
17301−2538	17 33 13.20	−25 40 22.0	PS	Y	Y	14.50 ± 0.07	13.88 ± 0.06	12.49 ± 0.06	
17361−4159	17 39 44.37	−42 00 39.7	PS	N	Y	15.68 ± 0.04	13.79 ± 0.04	11.701 ± 0.024	
17376−3448	17 40 56.36	−34 50 00.7	PS	N	Y	14.43 ± 0.06	13.54 ± 0.04	11.78 ± 0.03	
17382−2531	17 41 20.99	−25 32 49.1	PS	N	N	14.84 ± 0.06	13.90 ± 0.06	13.51 ± 0.06	
17393−2727	17 42 33.12	−27 28 24.9	PS	N	N	20.07 ± 0.20	18.13 ± 0.06	16.24 ± 0.04	4
17404−2713	17 43 38.07	−27 14 43.9	PS	N	N	16.32 ± 0.07	15.18 ± 0.15	14.33 ± 0.04	2
17418−3335	17 45 08.74	−33 36 07.4	PS	N	Y	15.57 ± 0.06	14.92 ± 0.04	13.50 ± 0.04	4
17443−2949	17 47 35.38	−29 50 53.2	E?	N	N	18.47 ± 0.24	17.33 ± 0.19	15.84 ± 0.27	
17479−3032	17 51 12.17	−30 33 40.7	PS	N	Y	15.00 ± 0.04	13.08 ± 0.04	12.029 ± 0.027	4
17482−2501	17 51 22.82	−25 01 53.4	PS	N	N	15.00 ± 0.06	13.87 ± 0.04	13.03 ± 0.04	
17487−1922	17 51 44.95	−19 23 43.4	PS	Y	Y	14.08 ± 0.04	13.37 ± 0.04	12.667 ± 0.028	2, 6
17506−2955	17 53 48.95	−29 55 42.8	PS	N	Y	10.47 ± 0.04	9.35 ± 0.04	8.826 ± 0.026	4
17543−3102	17 57 33.58	−31 03 02.1	PS	N	N	14.79 ± 0.07	14.19 ± 0.07	13.22 ± 0.06	6
17550−2120	17 58 04.94	−21 21 08.2	PS	N	N	>22.7	18.72 ± 0.09	16.76 ± 0.06	4
17552−2030	17 58 16.78	−20 30 17.8	PS	N	N	16.70 ± 0.05	15.71 ± 0.04	15.26 ± 0.04	
17560−2027	17 59 05.03	−20 27 25.0	PS	Y	Y	13.38 ± 0.07	12.24 ± 0.06	11.48 ± 0.06	4
18011−1847	18 04 02.36	−18 47 10.1	PS	N	N	19.03 ± 0.12	18.71 ± 0.09	16.35 ± 0.06	
18016−2743	18 04 45.65	−27 43 12.1	PS	N	N	>22.7	>21.8	15.03 ± 0.04	
18039−1903	18 06 53.26	−19 03 07.0	PS	N	N	22.1 ± 0.7	20.22 ± 0.11	18.42 ± 0.07	
18087−1440	18 11 34.13	−14 39 54.0	PS	N	Y	16.14 ± 0.04	13.84 ± 0.03	12.148 ± 0.024	4
18135−1456	18 16 25.79	−14 55 14.8	PS	N	N	>22.7	>21.8	15.88 ± 0.05	2
18246−1032	18 27 23.84	−10 30 23.2	PS	N	N	>22.5	>21.4	17.23 ± 0.07	4
18385+1350	18 40 51.80	+13 52 52.0	PS	N	N	16.401 ± 0.014	16.013 ± 0.016	15.523 ± 0.016	6
18514+0019	18 53 57.90	+00 23 28.4	PS	N	N	17.036 ± 0.023	14.911 ± 0.012	13.323 ± 0.014	4, 6
18580+0818	19 00 25.20	+08 22 47.6	PS	N	N	20.05 ± 0.10	18.33 ± 0.05	18.02 ± 0.04	
18596+0315	19 02 06.30	+03 20 16.1	PS	N	N	21.41 ± 0.13	17.72 ± 0.04	16.168 ± 0.023	
19013+0629	19 03 37.63	+06 34 09.3	PS	N	N	17.15 ± 0.04	15.711 ± 0.018	14.505 ± 0.016	

Table 5. continued.

IRAS name	α	δ	Spatial properties	DSS	2MASS	J	H	K	Ref.
	(J2000)	(J2000)				(mag)	(mag)	(mag)	
19015+1256	19 04 03.65	+13 01 51.2	PS	N	N	16.20 ± 0.03	14.115 ± 0.014	11.062 ± 0.014	
19071+0857	19 09 30.16	+09 02 25.7	E	N	Y	14.466 ± 0.011	13.136 ± 0.010	11.611 ± 0.012	4
19178+1206	19 20 14.01	+12 12 21.4	PS	N	Y	16.98 ± 0.04	14.921 ± 0.016	14.051 ± 0.020	
19190+1102	19 21 25.15	+11 08 42.0	PS	N	N	18.23 ± 0.12	16.53 ± 0.03	14.802 ± 0.017	
19208+1541	19 23 05.91	+15 47 31.5	PS	N	Y	13.493 ± 0.015	12.772 ± 0.011	10.517 ± 0.014	
19315+2235	19 33 41.50	+22 42 10.0	PS	N	N	19.13 ± 0.16	17.58 ± 0.09	16.52 ± 0.06	
19454+2920	19 47 24.39	+29 28 13.7	PS	N	N	17.30 ± 0.08	16.15 ± 0.05	15.2 ± 0.4	4, 6
20035+3242	20 05 30.02	+32 51 37.9	PS	N	Y	14.587 ± 0.011	13.823 ± 0.011	11.785 ± 0.011	
20042+3259	20 06 10.83	+33 07 50.5	PS	N	N	16.32 ± 0.04	15.82 ± 0.04	15.11 ± 0.03	6
21537+6435	21 55 04.65	+64 49 52.6	PS	N	N	20.51 ± 0.11	18.69 ± 0.05	15.788 ± 0.025	
21554+6204	21 56 58.18	+62 18 46.0	PS	N	N	20.96 ± 0.12	18.46 ± 0.06	11.848 ± 0.012	

Table 6. IRAS post-AGB star and PN candidates with dubious near-IR counterparts.

IRAS name	α	δ	$\Delta\alpha$	$\Delta\delta$	Distance	Spatial properties	J	H	K	Ref.
	(J2000)	(J2000)	($''$)	($''$)	($''$)		(mag)	(mag)	(mag)	
11544−6408-A	11 56 57.12	−64 25 16.8	0.0	2.9	2.9	PS	16.38 ± 0.04	15.95 ± 0.05	15.77 ± 0.04	6
11544−6408-B	11 56 56.95	−64 25 13.9	−1.1	0.0	1.1	E?	17.34 ± 0.06	16.60 ± 0.04	16.37 ± 0.05	6
17153−3814-A	17 18 45.54	−38 17 27.4	0.6	0.0	0.6	PS	11.67 ± 0.03	11.10 ± 0.04	10.83 ± 0.06	4
17153−3814-B	17 18 45.23	−38 17 25.1	4.2	−2.2	4.7	PS	13.15 ± 0.04	12.63 ± 0.04	12.25 ± 0.04	4

The narrow-band images were processed using standard IRAF routines. By comparing field stars in the emission line and continuum images, the contribution of continuum emission in the H_2 and Brγ images was found to be similar, within a few percent, to the emission detected in the K-continuum images. Images were consequently scaled by this small percentage before subtracting the continuum emission.

2.2. Archival data

As in Paper I, data were extracted from the Mid-course Space Experiment (MSX) Point Source Catalogue (MSX6C) and *Spitzer* Galactic Legacy Infrared Midplane Survey Extraordinaire (GLIMPSE) Image Atlas and source catalogues (Price et al. 2001; Fazio et al. 2004). A description of the data products extracted from these catalogues is given in Paper I.

To complement the mid-IR data, in this paper we have made also use of recently released AKARI data. AKARI is a Japanese space mission dedicated to infrared astronomical observations (Murakami et al. 2007) that has provided an all-sky survey in the 9 and 18 μm bands of the Infrared Camera (IRC, Onaka et al. 2007), and in the 65, 90, 140, and 160 μm bands of the Far-Infrared Surveyor (FIS, Kawada et al. 2007). We extracted data of the AKARI FIS Bright Source Catalogue and IRC Point Source Catalogue using the AKARI Catalogue Archive Server (AKARI-CAS)[5]. Only data for sources that are confirmed and whose flux is reliable, as indicated by a flux quality indicator FQUAL = 3, were used.

3. Objects with 2MASS PSC counterpart

The objects in our sample that have a counterpart in the 2MASS PSC were reported in Paper I. A comparison between the new JHK magnitudes determined from our NTT and TNG observations and these derived from the 2MASS PSC (Table 2 of Paper I) is mandatory in order to check the calibration of our observations and to assess the limits for point-source detection of the 2MASS PSC data. Furthermore, this comparison can uncover long term variability or it can be used to correct the 2MASS PSC magnitudes of objects that are contaminated by unresolved sources.

Figure 1 compares the JHK magnitudes derived from the NTT and TNG observations of the objects listed in Table 3 with the JHK magnitudes of the 2MASS PSC. The plots demonstrate that the JHK magnitudes derived from the NTT and TNG observations are consistent with the 2MASS PSC JHK magnitudes, thus giving support to the calibration of our JHK measurements. For objects fainter than ∼16 mag in J, ∼15 mag in H, and ∼14 mag in K, there is a clear deviation from the 1:1 relationship, with the J, H, and K magnitudes derived from our images being generally greater than the corresponding 2MASS PSC J, H, and K magnitudes. These deviations are consistent with the 2MASS PSC 10 σ detection limit for point-sources of J = 15.8 mag, H = 15.1 mag, and K_s = 14.3 mag (Skrutskie et al. 2006).

On the other hand, a number of objects show discrepancies larger than 10-σ between one of the new JHK magnitudes and the corresponding 2MASS PSC value. To verify the likely photometric variability of these sources, compiled in Table 4, we have compared the JHK magnitudes of a number of stars in their fields of view with their 2MASS PSC JHK magnitudes and confirmed that there are no systematic variations. We thus conclude that the variations reported for the sources in Table 4 are real.

The photometric variations in Table 4 fail to show consistent color changes that could be interpreted as post-AGB evolution if the sources were becoming bluer. Compared to the 2MASS values, the new TNG and NTT JHK magnitudes show that some of the sources are fainter, whereas others have become brighter.

---

[5] `http://darts.jaxa.jp/astro/akari/cas.html`

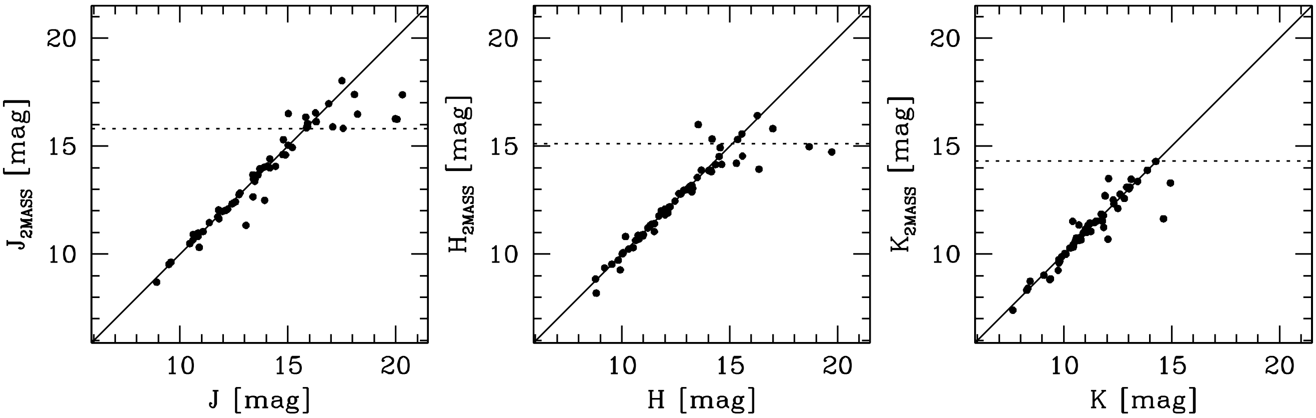

Fig. 1. *JHK* 2MASS PSC vs. NTT and TNG *JHK* magnitudes. In the plots, the solid line mark the 1:1 relationship and the dotted horizontal lines the 2MASS PSC 10-σ limiting magnitudes J = 15.8 mag, H = 15.1 mag, and K_s = 14.3 mag Sources above these lines are detected below the 10-σ. The error bars have not been plotted as they are in most cases smaller than the data points.

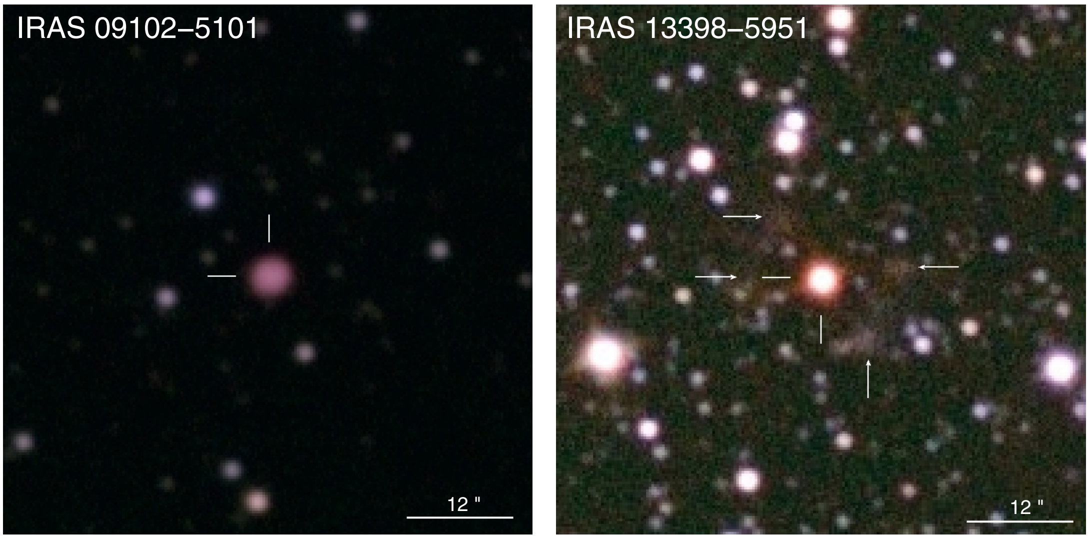

Fig. 2. J (blue), H (green), and K_S (red) composite pictures of IRAS 09102−5101 (*left*) and IRAS 13398−5951 (*right*). The new *JHK*$_s$ images show that these two objects, that already had 2MASS PSC counterpart, are extended. North is up, east to the left, and the locations of the near-IR counterparts are indicated by lines. The arrows on the picture of IRAS 13398−5951 mark the location of faint diffuse emission.

These brightness variations can be attributed to pulsation (e.g. Hrivnak et al. 2010) rather than to evolution. We note that, even if the IRAS variability of these sources is not large enough to have them excluded from our sample (see selection criteria in Paper I), they could still be variable stars. Additionally, IRAS 14104−5819, IRAS 18071−1727, and IRAS 18105−1935 show OH masers (te Lintel Hekkert et al. 1991; Sevenster et al. 2001) that might make them belong to the group of OH/IR AGB stars.

3.1. Extended sources among the objects with 2MASS PSC counterpart

The new *JHK* images have unveiled extended emission from IRAS 09102−5101 and IRAS 13398−5951 (Fig. 2), two sources whose near-IR counterparts had already been reported in Paper I. IRAS 09102−5101 shows a round nebula ∼2.″2 in radius that cannot be resolved in 2MASS images. Meanwhile, IRAS 13398−5951 displays low surface brightness extended emission, too faint to be detected in 2MASS images, which seems to be distributed in a discontinuous round shell, ∼10″ in radius, centered at the source.

4. Source identification

According to the procedure described in Paper I, we have primarily used the *Spitzer* GLIMPSE Image Atlas and catalogue to determine the accurate position of the objects with no 2MASS PSC counterpart. The images of the 29 objects in the *Spitzer* GLIMPSE Image Atlas are shown in Fig. 3. In all cases but IRAS 17153−3814, the identification of the *Spitzer* mid-IR counterpart of the IRAS post-AGB star and PN candidates is undoubtful.

When *Spitzer* GLIMPSE images were not available, we took advantage of the improved positional accuracy of the sources in the AKARI IRC catalogue to refine the IRAS coordinates of our target list. After the cross-correlation of IRAS and AKARI IRC coordinates, we found AKARI counterparts within 30″ of all IRAS sources but for IRAS 17153−3814 and IRAS 17479−3032, which are otherwise detected in *Spitzer* GLIMPSE images, and IRAS 17097−3624, for which a reddened near-IR counterpart is found at the location of the IRAS coordinates. For those sources that still lack an unambiguous near-IR counterpart, we examined the recently released

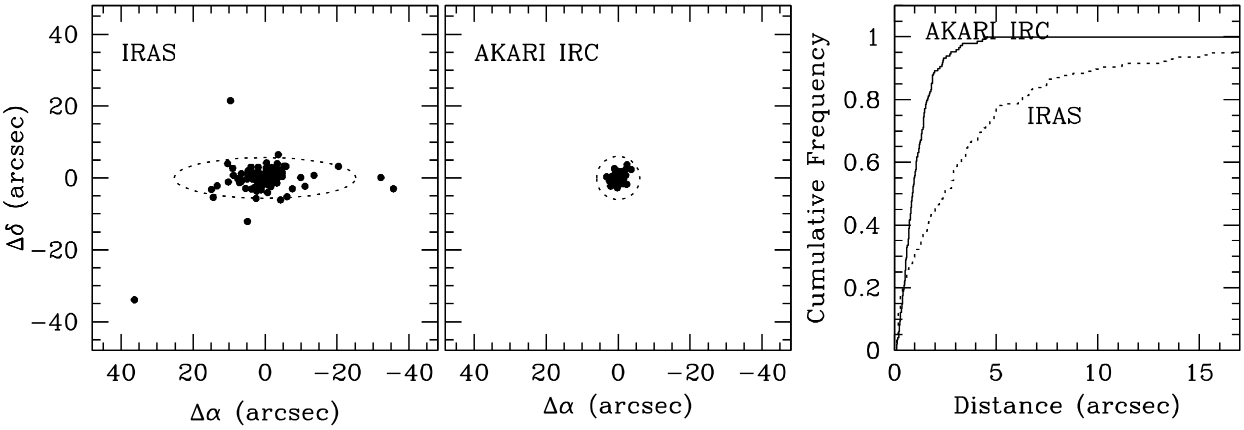

Fig. 6. Angular distance between the IRAS (*left*) and AKARI IRC (*center*) coordinates and the new near-IR coordinates derived in this work. The dashed figures corresponds to the median IRAS error ellipse and AKARI IRC positional uncertainty of the sources in our sample. (*Right*) Cumulative frequency of the distribution of the angular distance between the IRAS (dotted histogram) and AKARI IRC (solid histogram) coordinates and the new near-IR coordinates derived in this work.

Table 7. IRAS post-AGB star and PN candidates with no near-IR counterparts.

IRAS name	α (J2000)	δ (J2000)	Ref.
09370−4826	09 38 54.2	−48 40 16	6
16558−3417	16 59 09.6	−34 22 02	
17088−4221	17 12 22.9	−42 25 10	4
17385−2413	17 41 38.5	−24 14 35	
18051−2415	18 08 12.8	−24 14 36	
18083−2155	18 11 19.4	−21 55 04	6
18113−2503	18 14 26.74	−25 02 54.8	6
18529+0210	18 55 26.24	+02 14 46.4	
19011+1049	19 03 29.4	+10 53 51	

Wide-field Infrared Survey Explorer (WISE, Wright et al. 2010) images and searched for them in the WISE All-Sky Source Catalog.

All the objects that have been unambiguously identified are listed in Table 5. The table includes the improved coordinates, as derived from our near-IR observations (Cols. 2 and 3), a comment on the spatial properties of the source, describing whether it is extended or a point-source (Col. 4), a note on their detection on DSS red or 2MASS images (Cols. 5 and 6), the *JHK* magnitudes derived from the new observations (Cols. 7–9), and the reference to previous *JHK* measurements as listed in Table 3.

The two objects that have multiple possible counterparts within the AKARI IRC and IRAS error boxes, IRAS 11544−6408 and IRAS 17153−3814, are listed in Table 6. This table lists the near-IR coordinates of the possible counterparts and their positional offset with respect to the AKARI IRC coordinates for IRAS 11544−6408 and to the IRAS coordinates for IRAS 17153−3814 (Cols. 2–6), information on the extended nature of the sources (Col. 7), and our *JHK* magnitudes and references of previous measurements (Cols. 8–11). From the near-IR images at an angular resolution of 1.″0, it is unclear whether a number of unresolved stars is found at the location of IRAS 11544−6408-B, or whether it is extended.

Sources that do not have an evident near-IR counterpart within the AKARI IRC and IRAS error boxes are listed in Table 7. For these objects we provide their AKARI IRC coordinates, except for IRAS 18113−2503 and IRAS 18529+0210. For IRAS 18113−2503 we provide the source coordinates derived from the water maser structure detected with EVLA by Gómez et al. (2011). The absolute error of this position is 1.″2, whereas for IRAS 18529+0210, detected in all *Spitzer* IRAC bands, the *Spitzer* coordinates listed in Table 7 are known with an accuracy better than 2″. Despite the accurate positioning of these two sources, they have not been detected in our near-IR images, with detection limits $J > 22.5$ mag, $H > 21.4$ mag, and $K > 20.2$ mag, suggesting that they are highly obscured sources.

Composite pictures of the broad-band near-IR images of the sources in Table 5 are presented in Fig. 4. The location of the near-IR counterparts are overlaid on the pictures. The sources with multiple possible counterparts or with unidentified counterparts listed in Tables 6 and 7 are presented in Fig. 5. For sources with multiple possible counterparts, these different counterparts are labeled. When no counterpart was found, the IRAS ellipse error and AKARI IRC position error are overlaid.

4.1. IRAS, AKARI IRC and near-IR coordinates

The coordinates of the IRAS and AKARI sources are compared to these of their near-IR counterparts in Fig. 6. The rms of the difference between the IRAS coordinates is ∼17″ in right ascension and ∼5″ in declination, i.e., within the size of the median IRAS 1-σ error ellipse of our sample, 24″ × 6″. There are only 6 sources for which their near-IR and IRAS coordinates show a difference notoriously larger than the error ellipse of their IRAS coordinates. In these cases, an inspection of the original IRAS images revealed the presence of multiple nearby sources that, not being resolved by IRAS, resulted in an erroneous determination of the IRAS coordinates.

The comparison between the near-IR and AKARI IRC coordinates (Fig. 6-*center*) offers a sharper view. The rms of the difference between these coordinates is ≃1.″0 both in right ascension and declination. The cumulative frequency of the differences in coordinates (Fig. 6-*right*) shows that ∼90% of the sources have near-IR coordinates within 2″ of their AKARI IRC coordinates, whereas the same plot for the IRAS coordinates showed a greater dispersion.

4.2. Comparison with previous JHK measurements

There are 73 sources in our sample with previous *JHK* photometric measurements as listed in Tables 3, 5, 6, and 7.

Table 8. Extended post-AGB star and PN candidates.

IRAS name	Angular extent		Comments
	JHK (″)	IRAC† (″)	
05573+3156	25, 100	…	Multipolar PN or proto-PN candidate with one pair of inner bipolar lobes at PA ~ 45°–225° and one larger outer bipolar lobe at PA ~ 230°. Marked point-symmetry.
06499+0145	45	…	YSO candidate.
09102−5101	4.4	…	Round
12405−6219	35	60	Herbig-Haro candidate. Embedded within mid-IR diffuse emission
13398−5951	20	…	Detached discontinuous round shell
13404−6059	…	<0.5	Marginally resolved in the mid-IR 5.8 μm IRAC band
13500−6106	…	<0.9	Marginally resolved in the mid-IR 4.5 and 5.8 μm IRAC bands
15103−5754	8.4 × 6.3	1.7	Bipolar with symmetry axis along PA ~ 50°
15452−5459	13 × 10	180:	Hour-glass bipolar morphology with symmetry axis along PA ~ 45° Embedded within mid-IR nebular emission
15534−5422	5.5 × 3.7	2.4	Bipolar with symmetry axis along 140°
16333−4807	6.0 × 3.7	…	Bipolar with symmetry axis along PA ~ 0°
17009−4154	5.2 (*J*), 6.4 (*H*), 8.0 (*K*)	4.4	Round nebula
17150−3224	7.2 × 3.0	…	Bipolar, the Cotton Candy Nebula
17443−2949	…	~1.8	Marginally resolved in the mid-IR 4.5 μm IRAC band
18229−1127	…	2.1	Resolved in all IRAC bands
18454+0001	…	1.5	Resolved only in the mid-IR 8 μm IRAC band
18576+0341	…	4.6	Resolved in the mid-IR 3.6, 4.5, and 5.8 μm IRAC bands
19071+0857	7.4 × 3.5	1.7	Bipolar with symmetry axis along PA ~ 145°

Notes. (†) Deconvolved FWHM.

The comparison between the values of the *JHK* magnitudes in these tables and those in previous works is revealing: 28 out of the 73 sources in common have very similar *JHK* magnitudes, but the remaining 45 sources are considerably brighter in these previous works. Some of these works are based on observations carried out with a photometer (e.g., García-Lario et al. 1997) which may lead to the selection of an erroneous near-IR counterpart in crowded stellar regions using IRAS coordinates. Indeed, the inspection of the near-IR images of these objects in Fig. 4 confirms the presence of nearby bright sources that have certainly induced the misidentification of their counterparts in these works (e.g., IRAS 09370−4826 and IRAS 13500−6106). The use of 2MASS images has certainly improved the situation, but the limited sensitivity of 2MASS and the uncertainties in IRAS coordinates pose limits to this technique too, as was shown in Paper I.

5. Extended sources

We list in Table 8 the 18 sources found to be resolved or to present extended emission in near-IR *JHK* and/or mid-IR *Spitzer* IRAC images. Among these sources, 12 display extended emission in the near-IR, 6 show spatial profiles in mid-IR *Spitzer* IRAC images that are definitely inconsistent with those of point sources in their respective FoVs, and three others show indications of being marginally resolved at certain IRAC bands. For completeness, we also include IRAS 18229−1127, IRAS 18454+0001, and IRAS 18576+0341 that were already presented in Paper I as resolved in *Spitzer* IRAC images.

Near-IR narrow-band H_2, Brγ, and continuum images have been obtained for six of the sources listed in Table 8 as described in Sect. 2.2. The narrow-band images of these sources are presented in Fig. 7. According to the morphology seen in these images, and in the broad-band *JHK* (Fig. 4) and mid-IR *Spitzer* IRAC (Fig. 3), the extended sources can be classified into three different categories: young stellar object (YSOs) candidates, round post-AGB source and PN candidates, and bipolar post-AGB source and PN candidates. The objects in these categories are described in more detail below.

5.1. Young stellar object candidates

Among the sources with extended emission in our sample, IRAS 06499+0145 and IRAS 12405−6219 present irregular morphologies that do not fit the round/elliptical, bipolar, or multi-polar description typical of most post-AGB shells and young PNe (Sahai et al. 2011).

The broad-band *JHK* images of IRAS 06499+0145 (Fig. 4) show a resolved core embedded within diffuse emission, as well as a relatively bright blob and an arc-like filament are found ∼45″ southeast from the central source. The nature of this source is disputed as its IRAS fluxes place it in the region of the IRAS color–color diagram common to post-AGB stars (García-Lario et al. 1997) and ultra-compact H ii regions (Bronfman et al. 1996). The SEST detection of CS(2–1) molecular line emission (Bronfman et al. 1996) suggests a YSO nature, as this line is excited in the dense gas (10^4–10^5 cm^{-3}) typically found in the interior of molecular clouds, but its detection in AGB stars is rare (e.g., Olofsson et al. 1998). The abundance of CS decreases even further during the post-AGB and PN phases (Bachiller et al. 1997). Moreover, the LSR velocity of the CS emission, 45.1 km s^{-1} (Bronfman et al. 1996), is close to that of the molecular cloud [MAB97] 211.50+1.00 (47.6 km s^{-1}, May et al. 1997) whose projection on the sky encloses the IRAS source.

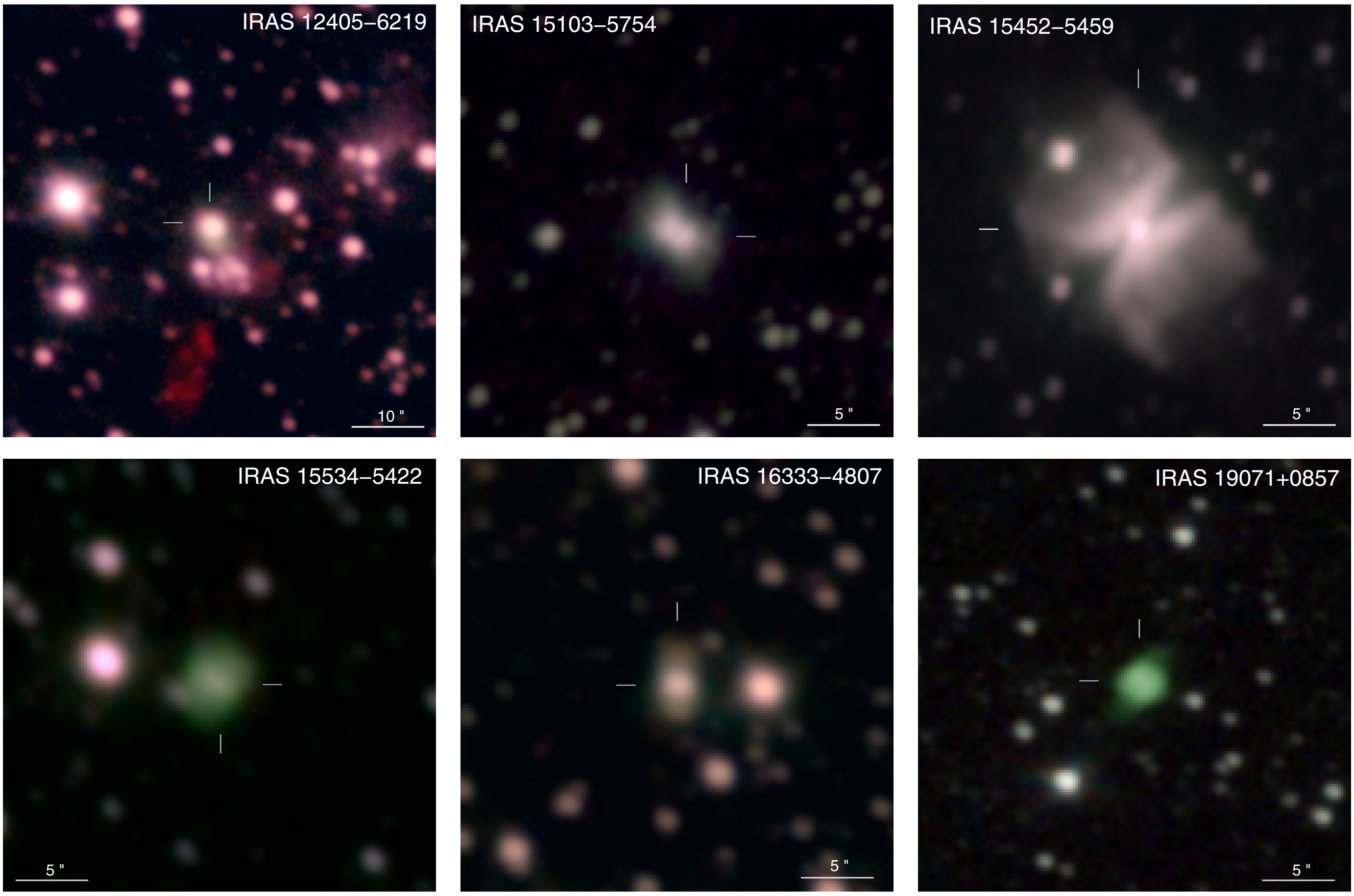

Fig. 7. H_2 (red), Brγ (green), and K continuum (blue) composite pictures of 6 sources with extended emission. The locations of the sources are indicated by lines. The field of view is 1′ for IRAS 12405−6219 and 30″ for the other sources. North is up, east to the left.

These evidences indicate that IRAS 06499+0145 is a young stellar object associated with the molecular cloud [MAB97] 211.50+1.00.

As for IRAS 12405−6219, its broad-band K_s image (Fig. 4) reveals a bright central source embedded within diffuse emission that, on the screen of our computer, extends up to ∼35″ along the direction at position angle ∼300° (measured north to east). Relatively bright knots of diffuse emission are also detected in the K_s band up to ∼11″ towards the south. Since these are the only patches of diffuse emission seen in the images around this source, it is likely that the diffuse emission is certainly associated to IRAS 12405−6219. Also the stars around IRAS 12405−6219 show a suspicious excess in the K_s image that may be indicative of a large absorption along the line of sight. The narrow-band near-IR images of IRAS 12405−6219 (Fig. 7) show a bright core with a patch of neutral material towards the northwest and south, similar to the K_s image. In addition, bright H_2 emission is detected up to ∼26″ towards the south of the central source. In the mid-IR (Fig. 3), the source appears embedded within bright 8 μm diffuse emission and shows a bright patch of 4.5 μm emission towards the south of the bright core which is spatially coincident with the bright patch of H_2 emission.

5.2. Round post-AGB source and PN candidates

There are three extended sources with round morphology: IRAS 09102−5101 and IRAS 13398−5951, presented in Fig. 2 and described in Sect. 3.2, and IRAS 17009−4154. The latter displays a round morphology in the near-IR JHK_s images (Fig. 4) with an angular size ∼5.″2 in J, ∼6.″4 in H, and ∼8.″0 in K_s, and resolved diffuse emission in the mid-IR *Spitzer* IRAC images (Fig. 3) at 3.6, 4.5, and 5.8 μm with a deconvolved PSF ∼4.″4 FWHM. Previous mid-IR N and near-IR K images presented by Van de Steene et al. (2000) showed a roundish faint nebulosity, 7″ in diameter, surrounding the star. Their near-IR K spectrum displays Brγ emission from ionized material, thus suggesting that the source has already reached the PN stage.

5.3. Bipolar post-AGB source and PN candidates

Seven sources are found to display bipolar morphology: IRAS 05573+3156, IRAS 15103−5754, IRAS 15452−5459, IRAS 15534−5422, IRAS 16333−4807, IRAS 17150−3224 (the Cotton Candy Nebula), and IRAS 19071+0857. These objects exhibit a variety of bipolar morphologies, with IRAS 15103−5754 and IRAS 15452−5459 (Fig. 4) displaying a dark equatorial region that marks a waist in their bipolar lobes, while IRAS 16333−4807, IRAS 17150−3224, and IRAS 19071+0857 (Fig. 4) display bright central regions from which fainter bipolar lobes protrude. The JHK' images of IRAS 05573+3156 (Fig. 4) show a bright core that is resolved along the direction at PA ∼ 45° and two bipolar lobes. The lobe along the southwest direction has an angular extent ∼90″, and bright emission at its tip, whereas the northeast lobe seems to lack emission on its east wall. Among the objects with bipolar morphology, only the bipolar lobes of IRAS 19071+0857 and IRAS 17150−3224 show some hints of point-symmetric brightness distribution.

Narrow-band H_2, Brγ, and K continuum images (Fig. 7) reveal prominent Brγ emission in IRAS 15534−5422 and IRAS 19071+0857. The ionization of their nebular material confirms they have reached the PN stage. On the other hand, the extended emission with bipolar morphology from IRAS 15103−5754, IRAS 15452−5459, and IRAS 16333−4807 is mainly continuum emission that can most likely be attributed to reflected emission from proto-PNe. The detection of radio continuum emission from IRAS 15103−5754 and IRAS 16333−4807 (Van de Steene & Pottasch 1993), however, suggests they are likely young PNe.

Two of the objects described above, IRAS 15452−5459 and IRAS 17150−3224, had been previously studied in detail. IRAS 15452−5459 has been described by Sahai et al. (2007) as an hourglass-shaped proto-PN using *HST* images in the *F814W* ACS filter and the *F110W*, *F160W*, and *F205W* NICMOS filters. Our *JHK* and H_2, Brγ and K continuum images confirm this morphology, including the narrow dark lane at the equatorial region separating the two bipolar lobes (Figs. 4 and 7). The *Spitzer* IRAC images of this source are remarkable (Fig. 3): the central region is barely resolved, but the source itself is found to be embedded within a region of diffuse emission with a 8 μm bright wavy filament crossing the source center. It is unclear whether this filament is related to IRAS 15452−5459, but a physical connection is suggested by its noticeable point-symmetry with respect to the source.

The proto-PN IRAS 17150−3224 has been amply studied (e.g., Kwok et al. 1998; Su et al. 2003; Hrivnak et al. 2006). The morphology revealed by our NTT *JHK* images is consistent with that shown in greater detail by previous broad-band optical and narrow- and broad-band near-IR *HST* images.

5.4. Morphology of resolved objects with water maser emission

In the case of O-rich sources, water maser emission has been claimed to trace the first signs of axisymmetric mass loss in the late evolutionary stages of the AGB and early post-AGB phase (Imai et al. 2002; Boboltz & Marvel 2005; Imai et al. 2007; Gómez et al. 2008; Suárez et al. 2009). Indeed, all post-AGB stars with water fountain characteristics (i.e., showing water maser components separated ≥100 km s^{-1}) and water-maser-emitting PNe whose optical or IR morphology have been resolved, are bipolar or highly axisymmetric: IRAS 16342−3814 (Sahai et al. 1999; Verhoelst et al. 2009), IRAS 17347−3139 (de Gregorio-Monsalvo et al. 2004), IRAS 18061−2505 (Suárez et al. 2006; Gómez et al. 2008), IRAS 19134+2131 (Imai et al. 2007), K 3-35 (Miranda et al. 2001), W43 A (Imai et al. 2002), and IRAS 15445−5449 (Pérez-Sánchez et al. 2011; Suárez et al., in prep.).

Among the seven objects of our sample that are resolved (Table 8), three display water maser emission[6]: IRAS 15103−5734 IRAS 15452−5459, and IRAS 16333−4807 (Deacon et al. 2007; Suárez et al. 2009). All these objects display IR bipolar morphologies, thus strengthening the hypothesis that water maser emission in post-AGB sources and PNe is associated with axisymmetric mass loss.

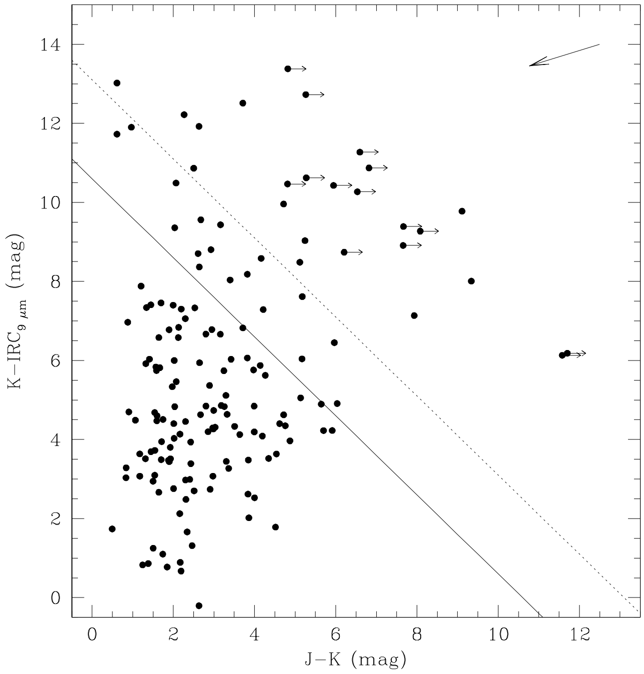

Fig. 8. Infrared color–color diagram for the post-AGB star and PN candidates in our sample. Sources above the dotted (solid) line have a $F_{9\,\mu\mathrm{m}}/F_J$ ratio larger than 1000 (100). The long arrow at the top right corner represents the shift in the position of a source on this plane after correcting it from a Galactic interstellar absorption of A_V = 10 mag The horizontal small arrows associated to some of the sources indicate that they are not detected in the J band and thus their location can still be shifted towards the right.

6. Obscured sources

We have compiled in Table 10 the *Spitzer* GLIMPSE 3.6, 4.5, 5.8, and 8.0 μm and MSX 8.28, 12.13, 14.65, and 21.3 μm fluxes extracted from the corresponding point source catalogs for the IRAS post-AGB star and PN candidates without 2MASS PSC counterpart in Paper I (Table 5 of Paper I provides this information for the IRAS sources with 2MASS PSC counterparts). Similarly, we list in Table 11 the AKARI IRC 9 and 18 μm and FIS 65, 90, 140, and 160 μm fluxes for these sources. Using these values, in conjunction with the IRAS fluxes from Table 1 of Paper I, and the NTT and TNG *JHK* magnitudes listed in Tables 3, 5, and 7, we have constructed the IR spectral energy distributions (SEDs) shown in Figs. 4 and 5.

The inspection of the individual IR SEDs of the IRAS post-AGB source and PN candidates in these figures discloses noticeable differences. Due to the selection criteria of this sample, most of the IR SEDs peak in the wavelength range 10–30 μm. Above 20 μm, the SED shows a steep decline for most sources, although there are a few of them that show a plateau extending at long wavelengths (e.g., IRAS 15534−5422). Below 20 μm, the SEDs of the sources in this sample show a great variety of shapes, showing a peak (e.g., IRAS 17548−2753), a flat shape (e.g., IRAS 17506−2955), a sharp decline (e.g., IRAS 18514+0019), or flux increase towards the shortest wavelengths in the JHK range (e.g., IRAS 18385+1350).

The most obscured sources can be selected among those whose SEDs show the steepest declines bluewards of 20 μm. The J and K magnitudes and the AKARI IRC 9 μm flux, which are available for most sources, can be used to select the most obscured objects. Figure 8 shows the distribution of the sources

---

[6] Water maser emission has also been detected in IRAS 12405−6219, but this object is likely to be a YSO candidate, as described in Sect. 5.1.

Table 9. List of obscured sources.

$F_{9\,\mu\mathrm{m}}/F_J > 1000$				
IRAS 08351−4634	IRAS 15284−6026	IRAS 17097−3624	IRAS 18039−1903	IRAS 18529+0210
IRAS 09370−4826	IRAS 15408−5657	IRAS 17168−3736	IRAS 18049−2118	IRAS 18596+0315
IRAS 10194−5625	IRAS 15531−5704	IRAS 17443−2949	IRAS 18113−2503	IRAS 21537+6435
IRAS 11549−6225	IRAS 16245−3859	IRAS 17550−2120	IRAS 18135−1456	IRAS 21554+6204
IRAS 13404−6059	IRAS 16518−3425	IRAS 18015−1352	IRAS 18199−1442	
IRAS 14104−5819	IRAS 16567−3838	IRAS 18016−2743	IRAS 18246−1032	
$1000 > F_{9\,\mu\mathrm{m}}/F_J > 100$				
IRAS 11444−6150	IRAS 13500−6106	IRAS 17393−2727	IRAS 18236−0447	IRAS 19178+1206
IRAS 11544−6408	IRAS 17021−3109	IRAS 18011−1847	IRAS 18580+0818	IRAS 19315+2235
IRAS 13293−6000	IRAS 17052−3245	IRAS 18071−1727	IRAS 19013+0629	IRAS 19454+2920

in the infrared color–color $J - K$ vs. $K - \mathrm{IRC}_{9\,\mu\mathrm{m}}$ diagram[7] Sources whose flux in the J band is 1000 (100) times fainter than at 9 μm are located above the dotted (solid) line in this diagram and are listed in Table 9. These sources represent the most obscured post-AGB and PN candidates in our sample. In particular, sources with $F_{9\,\mu\mathrm{m}}/F_J > 1000$ would be intrinsically 100 times fainter in the J band that at 9 μm and would still be located above the solid line in this diagram even if they suffered from a Galactic interstellar extinction of $A_\mathrm{V} = 10$ mag These are basically the sources undetected in the J band in Tables 3 and 5 and sources in Table 7 with no detectable near-IR source within their coordinate error boxes (i.e., IRAS 09370−4826, IRAS 18113−2503 and IRAS 18529+0210).

6.1. Galactic distribution of obscured sources

The Galactic distribution of different types of PNe and post-AGB stars is commonly used to assess the properties (mainly average initial mass) of their progenitors (e.g., Corradi & Schwarz 1995; Manchado et al. 2000; Stanghellini et al. 1993). Differences in Galactic height or latitude reported for elliptical/round and bipolar PNe (Corradi & Schwarz 1995; Stanghellini et al. 2002), and for SOLE (star-obvious low-level-elongated) and DUPLEX (dust-prominent longitudinally extended) post-AGB objects (Ueta et al. 2000; Siódmiak et al. 2008) have been interpreted as a result of bipolar PNe and DUPLEX post-AGB objects descending from high progenitor mass AGB stars.

It is thus interesting to study the location on Galactic coordinates of the sources with different degrees of obscuration (Fig. 9-*top*), and their Galactic latitude distributions (Fig. 9-*bottom*). Following Corradi & Schwarz (1995), we have fitted these distributions using an exponential fit $N = N_\mathrm{o}\mathrm{e}^{-b/\langle b\rangle}$, where $\langle b\rangle$ is the mean and standard deviation of this distribution. The widths of the best fits to these distribution, shown in Fig. 9-*bottom*, are 2°.0 for obscured ($F_{9\,\mu\mathrm{m}}/F_J > 100$) sources and 3°.0 for the less obscured sources ($F_{9\,\mu\mathrm{m}}/F_J < 100$). Similar fits have been computed for the samples of SOLE and DUPLEX sources (Ueta et al. 2000; Siódmiak et al. 2008), bipolar and elliptical PNe (Corradi & Schwarz 1995; Stanghellini et al. 2002), and optically bright post-AGB stars (Suárez et al. 2006). As shown in Fig. 9-*bottom*, these fits suggest that both our sample of obscured and less obscured sources and the sample of bipolar PNe and DUPLEX sources have almost indistinguishable Galactic latitude distributions with $\langle b\rangle$ equal to 2°.0, 3°.0, 2°.8 and 3°.3, respectively. Optically bright post-AGB stars and SOLE sources have slightly larger values of $\langle b\rangle$, 6°.6 and 7°.7, respectively, whereas the distribution of elliptical PNe has the largest width, 9°.3.

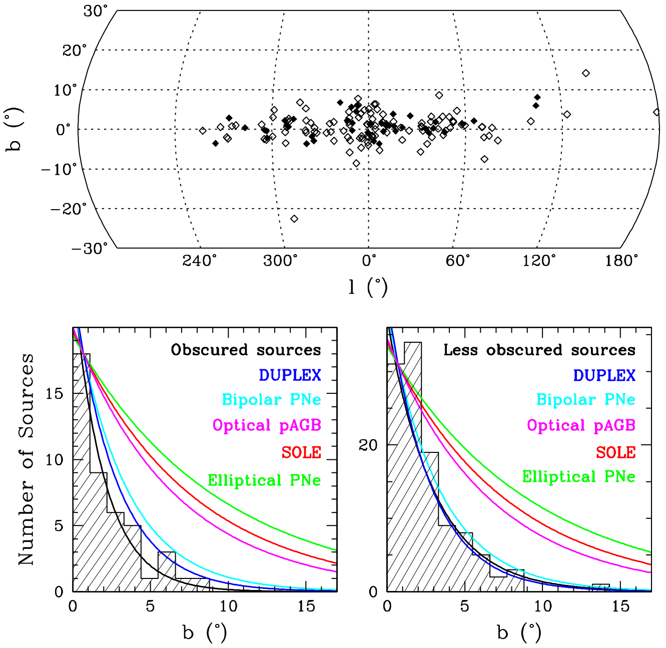

Fig. 9. (*Top*) Location in galactic coordinates of the sources in our sample. Obscured sources ($F_{9\,\mu\mathrm{m}}/F_J > 100$) are plotted with filled diamonds, whereas the open diamonds represent sources with lower obscuration ($F_{9\,\mu\mathrm{m}}/F_J < 100$). (*Bottom*) Galactic latitude distributions of obscured (*left*) and less obscured (*right*) sources in our sample. Exponential fits of these distributions, as described in the text, are shown by solid black lines. For comparison, similar fits (normalized to the first bin of the Galactic latitude distributions of obscured and unobscured sources) are shown for the samples of SOLE and DUPLEX sources of Siódmiak et al. (2008), for the samples of bipolar and elliptical PNe of Corradi & Schwarz (1995) and Stanghellini et al. (2002), and for the sample of optically bright post-AGB stars of Suárez et al. (2006).

To check whether the populations from which these samples are drawn are different or not, we have applied Kolmogorov-Smirnov statistical tests to each pair of samples. These tests did not show any significant statistical differences between

---

[7] The use of the IRAS 25 μm or AKARI IRC 18 μm fluxes, instead of the IRC 9 μm flux, results in very similar diagrams, but the shorter wavelength was selected because more objects have measurements in this band that at 18 μm and the accuracy of their fluxes is better than that of the IRAS 25 μm measurements.

Table 10. *Spitzer* and MSX fluxes of IRAS post-AGB star and PN candidates.

Object	Spitzer				MSX			
	3.6 μm [Jy]	4.5 μm [Jy]	5.8 μm [Jy]	8 μm [Jy]	8.28 μm [Jy]	12.13 μm [Jy]	14.65 μm [Jy]	21.3 μm [Jy]
IRAS 05573+3156	···	···	···	···	3.11 ± 0.13	9.3 ± 0.5	14.3 ± 0.5	36.3 ± 2.2
IRAS 06499+0145	···	···	···	···	0.382 ± 0.018	0.89 ± 0.08	1.61 ± 0.08	9.3 ± 0.6
IRAS 08351−4634	···	···	···	···	7.13 ± 0.3	16.4 ± 0.8	27.4 ± 0.8	31.1 ± 1.9
IRAS 09370−4826	···	···	···	···	5.87 ± 0.24	16.7 ± 0.8	24.6 ± 0.8	29.8 ± 1.8
IRAS 10194−5625	···	···	···	···	4.68 ± 0.19	16.8 ± 0.8	31.3 ± 0.8	41.0 ± 2.5
IRAS 11381−6401	···	···	···	···	1.51 ± 0.06	6.8 ± 0.3	11.9 ± 0.3	20.7 ± 1.2
IRAS 11444−6150	0.0076 ± 0.0004	0.0302 ± 0.0014	0.126 ± 0.003	0.632 ± 0.018	0.74 ± 0.03	2.54 ± 0.14	4.65 ± 0.14	9.7 ± 0.6
IRAS 11544−6408	···	···	···	···	10.3 ± 0.4	24.6 ± 1.2	34.1 ± 1.2	33.9 ± 2.0
IRAS 11549−6225	0.473 ± 0.026	···	9.3 ± 0.3	···	12.6 ± 0.5	18.6 ± 0.9	25.8 ± 0.9	28.6 ± 1.7
IRAS 12405−6219	···	···	···	···	5.92 ± 0.24	15.9 ± 0.8	25.0 ± 0.8	75 ± 5
IRAS 13293−6000	···	···	···	···	0.534 ± 0.024	0.74 ± 0.08	1.39 ± 0.08	2.7 ± 0.8
IRAS 13404−6059	0.00298 ± 0.00015	0.0388 ± 0.0016	0.330 ± 0.008	···	2.39 ± 0.10	7.4 ± 0.4	13.0 ± 0.4	15.0 ± 0.9
IRAS 13427−6531	···	···	···	···	0.127 ± 0.011	···	1.38 ± 0.03	4.3 ± 0.3
IRAS 13500−6106	0.00331 ± 0.00018	0.0372 ± 0.0016	0.273 ± 0.007	0.93 ± 0.03	0.599 ± 0.026	2.11 ± 0.12	4.40 ± 0.12	4.7 ± 0.3
IRAS 13529−5934	···	···	···	···	0.432 ± 0.020	1.67 ± 0.11	2.82 ± 0.11	7.7 ± 0.5
IRAS 15103−5754	0.264 ± 0.014	···	0.602 ± 0.017	1.096 ± 0.026	1.35 ± 0.06	9.8 ± 0.5	22.0 ± 0.5	58 ± 3
IRAS 15229−5433	···	···	···	···	0.172 ± 0.011	···	0.551 ± 0.010	2.04 ± 0.15
IRAS 15284−6026	···	···	···	···	0.391 ± 0.018	2.18 ± 0.13	5.53 ± 0.13	7.2 ± 0.4
IRAS 15452−5459	···	···	···	···	43.2 ± 1.8	101 ± 5	115 ± 5	193 ± 12
IRAS 15531−5704	···	···	···	···	0.73 ± 0.03	2.33 ± 0.14	3.43 ± 0.14	4.2 ± 0.3
IRAS 15534−5422	0.058 ± 0.007	0.057 ± 0.005	0.099 ± 0.007	0.202 ± 0.025	0.327 ± 0.015	1.29 ± 0.09	3.18 ± 0.09	4.4 ± 0.3
IRAS 16209−4714	···	···	···	···	0.214 ± 0.012	0.94 ± 0.09	2.92 ± 0.09	12.1 ± 0.7
IRAS 16296−4507	···	···	···	···	0.93 ± 0.04	3.62 ± 0.19	5.90 ± 0.19	11.4 ± 0.7
IRAS 16333−4807	0.171 ± 0.012	···	0.904 ± 0.021	···	3.29 ± 0.13	9.5 ± 0.5	15.0 ± 0.5	29.4 ± 1.7
IRAS 16507−4810	···	···	···	···	0.149 ± 0.010	···	1.69 ± 0.03	8.1 ± 0.5
IRAS 16518−3425	···	···	···	···	0.349 ± 0.019	···	1.95 ± 0.03	6.7 ± 0.4
IRAS 17009−4154	1.3 ± 0.3	1.33 ± 0.17	···	···	5.43 ± 0.23	7.3 ± 0.4	14.6 ± 0.4	70 ± 4
IRAS 17052−3245	···	···	···	···	1.10 ± 0.05	3.62 ± 0.21	5.17 ± 0.21	9.6 ± 0.6
IRAS 17067−3759	···	···	···	···	0.458 ± 0.020	2.16 ± 0.13	4.32 ± 0.13	7.6 ± 0.5
IRAS 17097−3624	···	···	···	···	0.459 ± 0.021	1.84 ± 0.12	3.83 ± 0.12	4.6 ± 0.3
IRAS 17150−3224	···	···	···	···	12.7 ± 0.5	61 ± 3	128 ± 3	247 ± 15
IRAS 17153−3814	0.0269 ± 0.0021	···	0.0173 ± 0.0012	···	0.408 ± 0.018	1.31 ± 0.09	3.07 ± 0.09	9.9 ± 0.6
IRAS 17158−4049	···	···	···	···	0.244 ± 0.012	1.27 ± 0.09	2.59 ± 0.09	4.8 ± 0.3
IRAS 17168−3736	0.035 ± 0.003	0.093 ± 0.007	0.440 ± 0.012	···	1.79 ± 0.07	10.1 ± 0.5	23.1 ± 0.5	24.9 ± 1.5
IRAS 17234−4008	···	···	···	···	0.195 ± 0.011	1.37 ± 0.09	3.68 ± 0.09	8.7 ± 0.5
IRAS 17301−2538	···	···	···	···	0.187 ± 0.012	···	1.22 ± 0.03	6.1 ± 0.4
IRAS 17376−3448	···	···	···	···	2.02 ± 0.08	3.54 ± 0.19	6.54 ± 0.19	8.4 ± 0.5
IRAS 17382−2531	···	···	···	···	2.06 ± 0.08	3.38 ± 0.18	6.01 ± 0.18	6.8 ± 0.4
IRAS 17393−2727	0.0086 ± 0.0005	0.0171 ± 0.0017	0.0360 ± 0.0011	0.229 ± 0.006	0.249 ± 0.012	1.04 ± 0.18	2.97 ± 0.18	10.7 ± 0.7
IRAS 17404−2713	0.0190 ± 0.0023	0.048 ± 0.003	0.161 ± 0.006	0.717 ± 0.023	0.72 ± 0.03	3.69 ± 0.20	8.30 ± 0.20	13.8 ± 0.8
IRAS 17418−3335	···	···	···	···	0.262 ± 0.014	1.75 ± 0.11	3.68 ± 0.11	9.6 ± 0.6
IRAS 17443−2949	0.071 ± 0.003	0.63 ± 0.1 0	8.2 ± 0.3	···	15.1 ± 0.6	22.5 ± 1.1	42.90 ± 1.13	39.5 ± 2.4
IRAS 17479−3032	0.0229 ± 0.0011	···	0.0638 ± 0.0016	0.273 ± 0.006	0.343 ± 0.017	···	2.82 ± 0.04	8.2 ± 0.5
IRAS 17482−2501	0.0117 ± 0.0009	0.0455 ± 0.0026	0.119 ± 0.004	0.380 ± 0.013	0.295 ± 0.014	0.96 ± 0.08	1.64 ± 0.08	3.13 ± 0.20
IRAS 17487−1922	···	···	···	···	0.82 ± 0.04	2.1 ± 0.13	4.51 ± 0.13	16.2 ± 1.0
IRAS 17506−2955	0.199 ± 0.021	0.365 ± 0.026	0.79 ± 0.03	1.40 ± 0.05	0.94 ± 0.04	1.20 ± 0.06	1.03 ± 0.06	1.00 ± 0.06
IRAS 17543−3102	···	···	···	···	0.475 ± 0.021	1.80 ± 0.10	4.89 ± 0.10	13.9 ± 0.8
IRAS 17550−2120	···	···	···	···	1.26 ± 0.05	5.1 ± 0.3	11.60 ± 0.27	15.7 ± 0.9
IRAS 17552−2030	···	···	···	···	0.230 ± 0.012	1.10 ± 0.08	2.21 ± 0.08	3.32 ± 0.21
IRAS 17560−2027	···	···	···	···	0.174 ± 0.011	1.11 ± 0.09	2.92 ± 0.09	10.1 ± 0.6
IRAS 18011−1847	···	···	···	···	0.75 ± 0.03	3.18 ± 0.17	6.02 ± 0.17	10.3 ± 0.6
IRAS 18016−2743	···	···	···	···	3.65 ± 0.15	4.65 ± 0.24	6.91 ± 0.24	8.0 ± 0.5
IRAS 18039−1903	0.0106 ± 0.0004	0.155 ± 0.006	1.15 ± 0.03	···	1.83 ± 0.08	3.30 ± 0.18	6.66 ± 0.18	6.0 ± 0.4
IRAS 18087−1440	···	···	···	···	0.353 ± 0.017	1.61 ± 0.11	5.66 ± 0.11	13.9 ± 0.8
IRAS 18135−1456	0.0257 ± 0.0012	0.165 ± 0.006	1.032 ± 0.023	···	4.61 ± 0.19	26.1 ± 1.3	59.0 ± 1.3	82 ± 5
IRAS 18246−1032	0.0322 ± 0.0013	0.189 ± 0.007	0.723 ± 0.022	1.45 ± 0.04	0.87 ± 0.04	2.39 ± 0.12	6.02 ± 0.12	12.3 ± 0.7
IRAS 18514+0019	0.0348 ± 0.0026	0.110 ± 0.005	0.332 ± 0.010	1.15 ± 0.03	1.05 ± 0.04	5.07 ± 0.26	9.99 ± 0.26	17.4 ± 1.0
IRAS 18529+0210	0.0047 ± 0.0003	0.095 ± 0.004	0.871 ± 0.023	···	4.17 ± 0.17	13.2 ± 0.7	21.0 ± 1.3	18.2 ± 1.1
IRAS 18580+0818	···	···	···	···	0.147 ± 0.009	1.00 ± 0.08	1.60 ± 0.08	2.90 ± 0.19
IRAS 18596+0315	0.0097 ± 0.0005	0.0482 ± 0.0015	0.212 ± 0.006	0.801 ± 0.015	0.484 ± 0.021	2.94 ± 0.16	6.19 ± 0.16	9.3 ± 0.6
IRAS 19013+0629	0.0245 ± 0.0011	0.111 ± 0.005	0.408 ± 0.012	1.50 ± 0.06	1.40 ± 0.06	4.23 ± 0.22	7.99 ± 0.22	11.5 ± 0.7
IRAS 19015+1256	···	···	···	···	1.18 ± 0.05	1.81 ± 0.11	2.02 ± 0.11	2.61 ± 0.18
IRAS 19071+0857	0.0345 ± 0.0021	0.058 ± 0.004	0.055 ± 0.005	0.251 ± 0.016	0.446 ± 0.020	1.24 ± 0.09	4.22 ± 0.09	11.1 ± 0.7
IRAS 19178+1206	0.118 ± 0.004	···	2.162 ± 0.034	4.61 ± 0.14	2.11 ± 0.09	4.51 ± 0.23	6.22 ± 0.23	7.0 ± 0.4
IRAS 19190+1102	···	···	···	···	0.120 ± 0.010	1.18 ± 0.09	3.45 ± 0.09	8.1 ± 0.5
IRAS 19208+1541	0.240 ± 0.009	0.379 ± 0.022	0.479 ± 0.011	0.513 ± 0.012	0.4 ± 0.019	···	0.687 ± 0.020	···
IRAS 19315+2235	···	···	···	···	0.297 ± 0.015	1.43 ± 0.10	2.48 ± 0.10	4.2 ± 0.3
IRAS 19454+2920	···	···	···	···	4.52 ± 0.19	19.0 ± 1.0	41.1 ± 1.0	65 ± 4
IRAS 20035+3242	···	···	···	···	3.69 ± 0.15	8.1 ± 0.4	11.8 ± 0.4	18.4 ± 1.10
IRAS 20042+3259	···	···	···	···	0.498 ± 0.022	1.34 ± 0.09	2.40 ± 0.09	2.35 ± 0.16

Table 11. AKARI fluxes of IRAS post-AGB star and PN candidates.

Object	AKARI IRC		AKARI FIS			
	9 μm [Jy]	18 μm [Jy]	65 μm [Jy]	90 μm [Jy]	140 μm [Jy]	160 μm [Jy]
IRAS 04137+7016	0.365	1.465	…	0.829	…	…
IRAS 05573+3156	3.977	28.165	87.614	72.051	87.821	117.814
IRAS 06499+0145	0.460	6.120	26.097	29.332	40.311	35.789
IRAS 08351−4634	6.756	31.556	12.925	9.830	2.821	…
IRAS 09370−4826	10.560	34.657	12.456	8.871	…	…
IRAS 10194−5625	5.571	40.687	…	…	…	…
IRAS 11381−6401	1.875	17.098	…	8.244	…	…
IRAS 11444−6150	0.840	7.264	10.952	…	…	…
IRAS 11549−6225	4.978	16.432	8.070	4.586	…	…
IRAS 12405−6219	7.880	59.992	…	…	…	…
IRAS 13293−6000	0.466	1.067	5.269	5.984	…	…
IRAS 13404−6059	2.462	13.505	…	5.974	…	…
IRAS 13427−6531	0.176	2.768	…	1.935	…	…
IRAS 13500−6106	0.751	4.907	…	4.802	…	…
IRAS 13529−5934	0.471	5.433	…	4.751	…	…
IRAS 14249−5310	1.847	6.120	11.947	9.954	…	…
IRAS 15103−5754	1.258	39.298	124.595	…	57.557	44.747
IRAS 15229−5433	0.169	1.533	…	…	…	…
IRAS 15284−6026	0.338	5.607	8.543	5.822	…	…
IRAS 15452−5459	44.849	171.435	…	…	…	…
IRAS 15531−5704	0.681	4.051	…	1.535	…	…
IRAS 15534−5422	0.356	3.509	8.818	7.144	9.399	…
IRAS 16209−4714	0.301	8.554	…	…	…	…
IRAS 16245−3859	1.867	12.836	…	18.864	7.280	…
IRAS 16296−4507	1.022	8.832	11.451	6.927	…	…
IRAS 16333−4807	3.620	23.088	99.218	50.042	24.706	…
IRAS 16507−4810	0.158	5.032	…	5.448	…	…
IRAS 16518−3425	0.424	5.051	…	0.909	…	…
IRAS 17009−4154	5.304	45.000	63.494	26.417	…	…
IRAS 17052−3245	1.218	7.450	9.356	8.898	…	…
IRAS 17067−3759	0.562	6.158	…	5.274	…	…
IRAS 17150−3224	…	195.873	…	…	41.169	…
IRAS 17158−4049	0.281	3.593	…	…	…	…
IRAS 17168−3736	1.508	21.088	47.068	24.872	…	…
IRAS 17234−4008	0.253	6.095	8.432	6.765	…	…
IRAS 17301−2538	0.249	3.452	3.397	2.614	…	…
IRAS 17361−4159	1.795	4.918	…	3.633	…	…
IRAS 17376−3448	1.980	7.014	…	…	…	…
IRAS 17382−2531	1.459	4.658	…	1.932	…	…
IRAS 17393−2727	0.255	6.900	…	…	…	…
IRAS 17404−2713	…	10.778	17.111	…	…	…
IRAS 17418−3335	…	6.404	16.861	9.474	…	…
IRAS 17443−2949	11.638	36.291	…	…	…	…
IRAS 17482−2501	0.358	…	…	6.236	…	16.030
IRAS 17487−1922	0.948	…	…	3.575	…	…
IRAS 17506−2955	1.468	1.611	…	…	…	…
IRAS 17543−3102	…	9.738	19.050	11.920	…	…
IRAS 17550−2120	…	12.029	26.236	18.381	…	…
IRAS 17552−2030	0.311	2.934	…	…	…	…
IRAS 18011−1847	0.824	…	…	…	…	…
IRAS 18016−2743	2.362	6.950	…	…	…	…
IRAS 18039−1903	1.848	6.474	…	…	…	…
IRAS 18087−1440	0.512	10.379	21.748	16.356	…	19.076
IRAS 18135−1456	4.233	71.694	142.350	54.734	47.544	36.399
IRAS 18246−1032	0.974	…	38.461	21.440	…	…
IRAS 18385+1350	0.161	1.765	…	1.938	…	…
IRAS 18514+0019	1.074	…	22.469	12.401	…	…
IRAS 18580+0818	…	2.051	…	…	…	…
IRAS 18596+0315	0.598	7.817	15.153	16.854	15.379	…
IRAS 19013+0629	1.497	9.507	13.762	7.619	11.094	…
IRAS 19015+1256	1.687	2.909	…	0.790	…	…
IRAS 19071+0857	0.463	7.678	18.683	7.292	…	…
IRAS 19178+1206	3.402	9.185	…	2.553	…	…
IRAS 19190+1102	0.132	6.100	17.670	12.904	…	9.638
IRAS 19208+1541	0.449	0.796	…	…	…	…
IRAS 19315+2235	0.318	3.239	…	2.028	…	…
IRAS 19454+2920	5.428	56.548	38.652	21.621	5.988	…
IRAS 20035+3242	3.836	15.414	13.803	12.531	…	…
IRAS 20042+3259	0.547	2.592	…	…	…	…
IRAS 21537+6435	1.992	17.201	8.875	6.823	…	…
IRAS 21554+6204	63.465	127.303	44.182	24.448	6.131	…

the Galactic latitude distributions of the samples of obscured and less obscured sources, bipolar PNe and DUPLEX sources, whereas these distributions are distinct at a 95% confidence level from those of optically bright post-AGB stars, elliptical PNe and SOLE sources (the latter only marginally owing probably to the small size of this sample). The obscured and less obscured sources in our sample and the stellar progenitors of bipolar PNe and DUPLEX sources may arise from the same population of sources, which seems to be different from those of the stellar progenitors of optically bright post-AGB stars, SOLE sources and elliptical PNe.

7. Summary

This is the second paper in a series aimed at investigating the spectral properties and determining the nature of a sample of 165 presumably obscured IRAS post-AGB star and PN candidates. In Paper I (Ramos-Larios et al. 2009), 2MASS, MSX and *Spitzer* GLIMPSE archival data were used to search for near-IR counterparts in the 2MASS PSC, but the limited sensitivity of 2MASS observations did not allow the identification of ~80 sources in the sample.

To overcome this problem, near-IR JHK images have been obtained for 164 objects in the sample of IRAS post-AGB star and PN candidates. The new near-IR JHK images, in conjunction with MSX, *Spitzer* GLIMPSE and recently available AKARI archival data, have allowed the unambiguous identification of near-IR counterparts for 154 out of the 165 sources in the sample. Accurate finding charts are provided in this paper for the sources lacking a PSC counterpart, thus complementing those presented in Paper I for the sources with PSC counterparts.

We have selected the sources with the greatest obscuration degree between the mid-IR 9 μm band and the near-IR J band. The Galactic latitude distribution of these sources, close to the Galactic Plane, is consistent with that of bipolar PNe and DUPLEX sources, and thus it does not disproof the possible link between obscured post-AGB stars and PNe, high progenitor mass AGB stars and bipolar PNe.

Sources that have a near-IR 2MASS PSC counterpart have also been investigated for long-term variability. The JHK magnitudes of a dozen sources have been found to have varied between the time of the 2MASS observations and that of the NTT and TNG observations. The color changes implied by these variations are not consistent with post-AGB evolution, but they can be rather interpreted as the result of pulsation.

Extended or resolved emission has been found in 18 objects and near-IR Brγ, H$_2$, and K continuum images have been obtained for 6 of them. Among these sources, IRAS 06499+0145 and IRAS 12405−6219 are proposed to be young stellar object candidates, and 10 sources are proposed to be post-AGB source and PN candidates with either round (IRAS 09102−5101, IRAS 13398−5951, and IRAS 17009−4154) or bipolar (IRAS 05573+3156, IRAS 15103−5754, IRAS 15452−5459, IRAS 15534−5422, IRAS 16333−4807, IRAS 19071+0857, and IRAS 17150−3224) morphologies. The detection of near-IR Brγ line emission or radio continuum suggests that IRAS 15103−5754, IRAS 15534−5422, IRAS 16333−4807, IRAS 17009−4154, and IRAS 19071+0857 have already reached the PN stage.

We find that all sources in our sample that are resolved and have water maser emission are bipolar. This strengthens the hypothesis that water maser emission is associated with axisymmetric mass loss in evolved stars.

Acknowledgements. This research has made use of: the SIMBAD database, operated at CDS, Strasbourg, France, data products from the 2MASS, which is a joint project of the University of Massachusetts and the Infrared Processing and Analysis Center/California Institute of Technology, funded by the National Aeronautics and Space Administration and the National Science Foundation, and data based on observations obtained with AKARI, a JAXA project with the participation of ESA, and on observations made with the *Spitzer* Space Telescope, which is operated by the Jet Propulsion Laboratory, California Institute of Technology under a contract with NASA. Support for this work was provided by an award issued by JPL/Caltech. G.R.L. acknowledges support of a postdoctoral fellowship from CONACyT (Mexico) grant 75861. Important support has been provided by several grants of the Spanish Ministerio de Ciencia e Innovación (MICINN): AYA2008-01934 (GRL, LFM, MAG, and OS), AYA2008-06189-C03-01 (JFG and OS), AYA2011-29754-C03-02 (MAG), and AYA 2011-30228-C03-01 (JFG, LFM, and OS). J.F.G., M.A.G., and L.F.M. acknowledge partial support of grant TIC-126 from Consejería de Innovación, Ciencia y Empresa of Junta de Andalucía. L.F.M. is supported partially by grants INCITE09E1R312096ES and INCITE09312191PR of the Galician INCITE research program of the Dirección Xeral de Investigación, Desenvolvemento y Innovación of the Spanish Xunta de Galicia. Finally, we thank Martin Cohen for helpful discussion on the accuracy of *Spitzer* GLIMPSE data.

References

Bachiller, R., Forveille, T., Huggins, P. J., & Cox, P. 1997, A&A, 324, 1123
Baffa, C., Comoretto, G., Gennari, S., et al. 2001, A&A, 378, 722
Blöcker, T. 1995a, A&A, 297, 727
Blöcker, T. 1995b, A&A, 299, 755
Boboltz, D. A., & Marvel, K. B. 2005, ApJ, 627, L45
Bronfman, L., Nyman, L.-Å., & May, J. 1996, A&AS, 115, 81
Corradi, R. L. M., & Schwarz, H. E. 1995, A&A, 293, 871
de Gregorio-Monsalvo, I., Gómez, Y., Anglada, G., et al. 2004, ApJ, 601, 921
Deacon, R. M., Chapman, J. M., Green, A. J., & Sevenster, M. N. 2007, ApJ, 658, 1096
Fazio, G. G., Hora, J. L., Allen, L. E., et al. 2004, ApJS, 154, 10
García-Lario, P., Manchado, A., Suso, S. R., Pottasch, S. R., & Olling, R. 1990, A&AS, 82, 497
García-Lario, P., Manchado, A., Pych, W., & Pottasch, S. R. 1997, A&AS, 126, 479
Gómez, J. F., Suárez, O., Gómez, Y., et al. 2008, AJ, 135, 2074
Gómez, J. F., Rizzo, J. R., Suárez, O., et al. 2011, ApJ, 739, L14
Hoogzaad, S. N., Molster, F. J., Dominik, C., et al. 2002, A&A, 389, 547
Hrivnak, B. J., Kelly, D. M., Su, K. Y. L., Kwok, S., & Sahai, R. 2006, ApJ, 650, 237
Hrivnak, B. J., Lu, W., Maupin, R. E., & Spitzbart, B. D. 2010, ApJ, 709, 1042
Hunt, L. K., Mannucci, F., Testi, L., et al. 1998, AJ, 115, 2594
Imai, H., Obara, K., Diamond, P. J., Omodaka, T., & Sasao, T. 2002, Nature, 417, 829
Imai, H., Sahai, R., & Morris, M. 2007, ApJ, 669, 424
Jiménez-Esteban, F. M., García-Lario, P., Engels, D., & Manchado, A. 2006a, A&A, 458, 533
Jiménez-Esteban, F. M., García-Lario, P., Engels, D., & Perea Calderón, J. V. 2006b, A&A, 446, 773
Kawada, M., Baba, H., Barthel, P. D., et al. 2007, PASJ, 59, S389
Kwok, S., Su, K. Y. L., & Hrivnak, B. J. 1998, ApJ, 501, L117
May, J., Alvarez, H., & Bronfman, L. 1997, A&A, 327, 325
Miranda, L. F., Gómez, Y., Anglada, G., & Torrelles, J. M. 2001, Nature, 414, 284
Moorwood, A., Cuby, J.-G., & Lidman, C. 1998, The Messenger, 91, 9
Olofsson, H., Lindqvist, M., Nyman, L.-A., & Winnberg, A. 1998, A&A, 329, 1059
Onaka, T., Matsuhara, H., Wada, T., et al. 2007, PASJ, 59, S401
Manchado, A., Pottasch, S. R., García-Lario, P., Esteban, C., & Mampaso, A. 1989, A&A, 214, 139
Manchado, A., Villaver, E., Stanghellini, L., & Guerrero, M. A. 2000, Asymmetrical Planetary Nebulae II: From Origins to Microstructures, 199, 17
Murakami, H., Baba, H., Barthel, P., et al. 2007, PASJ, 59, S369
Pérez-Sánchez, A. F., Vlemmings, W. H. T., & Chapman, J. M. 2011, MNRAS, 418, 1402
Persson, S. E., Murphy, D. C., Krzeminski, W., Roth, M., & Rieke, M. J. 1998, AJ, 116, 2475
Pottasch, S. R., Olling, R., Bignell, C., & Zijlstra, A. A. 1988, A&A, 205, 248
Price, S. D., Egan, M. P., Carey, S. J., Mizuno, D. R., & Kuchar, T. A. 2001, AJ, 121, 2819
Ramos-Larios, G., Guerrero, M. A., Suárez, O., Miranda, L. F., & Gómez, J. F. 2009, A&A, 501, 1207

Sahai, R., te Lintel Hekkert, P., Morris, M., Zijlstra, A., & Likkel, L. 1999, ApJ, 514, L115
Sahai, R., Morris, M., Sánchez Contreras, C., & Claussen, M. 2007, AJ, 134, 2200
Sahai, R., Morris, M. R., & Villar, G. G. 2011, AJ, 141, 134
Schönberner, D. 1981, A&A, 103, 119
Sevenster, M. N. 2002, AJ, 123, 2772
Sevenster, M. N., van Langevelde, H. J., Moody, R. A., et al. 2001, A&A, 366, 481
Siódmiak, N., Meixner, M., Ueta, T., et al. 2008, ApJ, 677, 382
Skrutskie, M. F., Cutri, R. M., Stiening, R., et al. 2006, AJ, 131, 1163
Soker, N. 2008, ApJ, 674, L49
Stanghellini, L., Corradi, R. L. M., & Schwarz, H. E. 1993, A&A, 279, 521
Stanghellini, L., Villaver, E., Manchado, A., & Guerrero, M. A. 2002, ApJ, 576, 285
Su, K. Y. L., Hrivnak, B. J., Kwok, S., & Sahai, R. 2003, AJ, 126, 848
Suárez, O., García-Lario, P., Manchado, A., et al. 2006, A&A, 458, 173
Suárez, O., Gómez, J. F., Miranda, L. F., et al. 2009, A&A, 505, 217
Szczerba, R., Siódmiak, N., Stasińska, G., & Borkowski, J. 2007, A&A, 469, 799
te Lintel Hekkert, P., Caswell, J. L., Habing, H. J., Haynes, R. F., & Norris, R. P. 1991, A&AS, 90, 327
Ueta, T., Meixner, M., & Bobrowsky, M. 2000, ApJ, 528, 861
Van de Steene, G. C. M., & Pottasch, S. R. 1993, A&A, 274, 895
Van de Steene, G. C. M., van Hoof, P. A. M., & Wood, P. R. 2000, A&A, 362, 984
Van der Veen, W. E. C. J., Habing, H. J., & Geballe, T. R. 1989, A&A, 226, 108
Vassiliadis, E., & Wood, P. R. 1993, ApJ, 413, 641
Verhoelst, T., Waters, L. B. F. M., Verhoeff, A., et al. 2009, A&A, 503, 837
Wainscoat, R. J., & Cowie, L. L. 1992, AJ, 103, 332
Wright, E. L., Eisenhardt, P. R. M., Mainzer, A. K., et al. 2010, AJ, 140, 1868

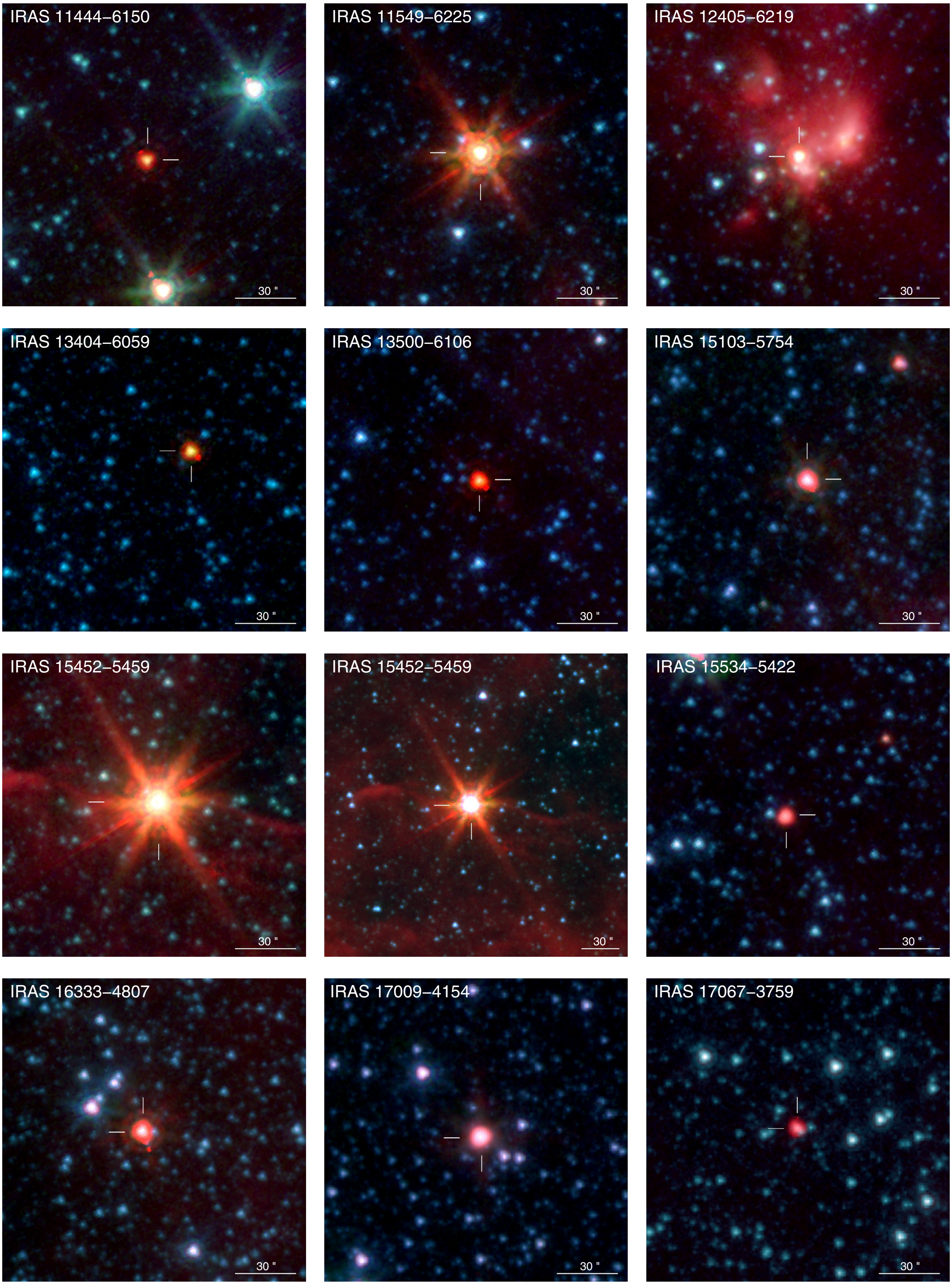

Fig. 3. *Spitzer* GLIMPSE composite pictures of the IRAS post-AGB star and PN candidates with no near-IR counterparts in the 2MASS PSC (Paper I). The blue, green, and red colors in the composite pictures correspond to the 3.6 μm, 4.5 μm, and 8.0 μm bands, respectively, but for IRAS 17009−4154, IRAS 17443−2949, IRAS 18135−1456, and IRAS 18529+0210, for which their saturated 8 μm images were replaced in the red channel by the 5.8 μm images, and for IRAS 17067−3759, for which blue and green correspond to 4.5 μm. The locations of the sources are overlaid on the pictures. North is up, east to the left.

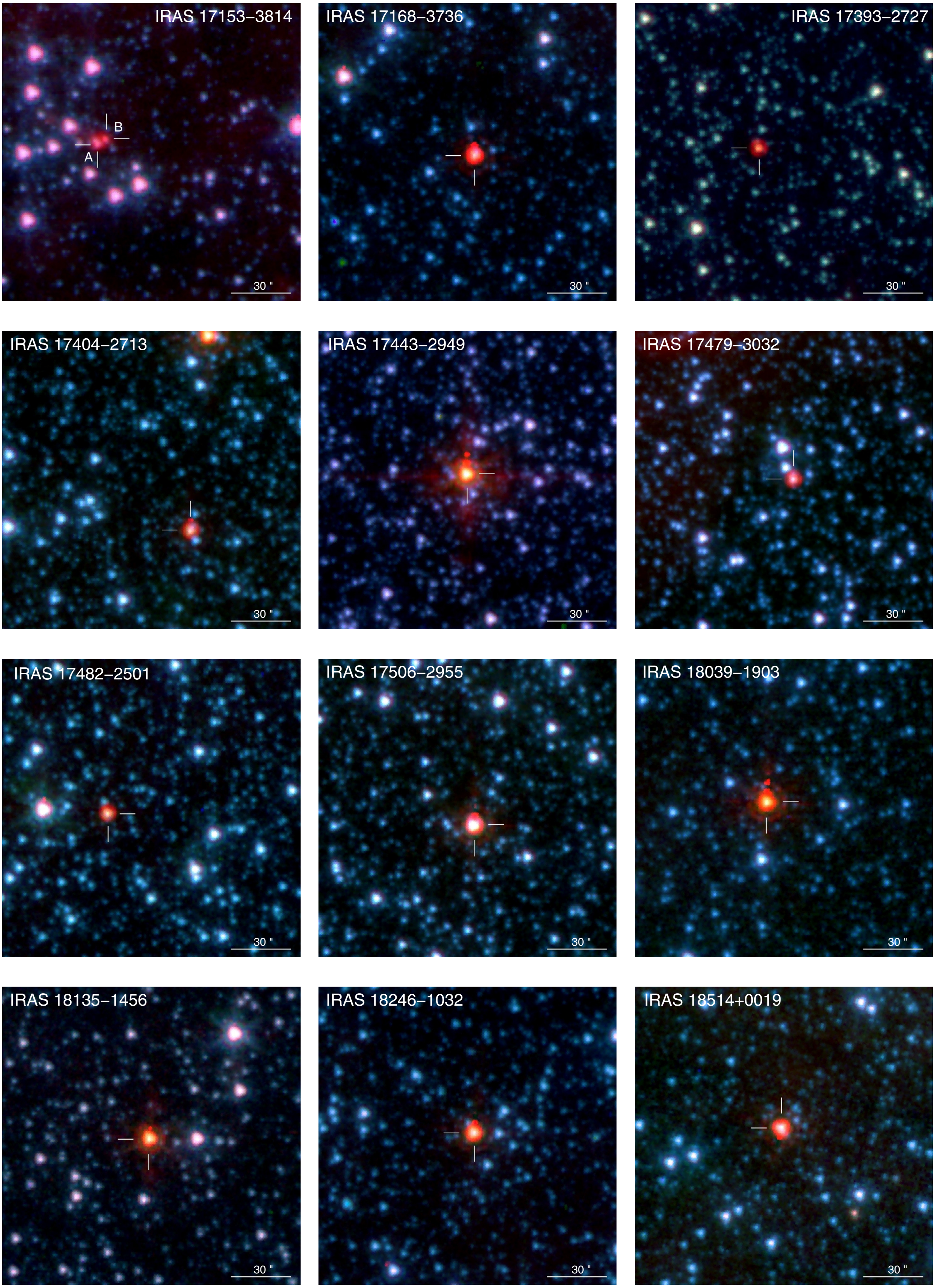

Fig. 3. continued.

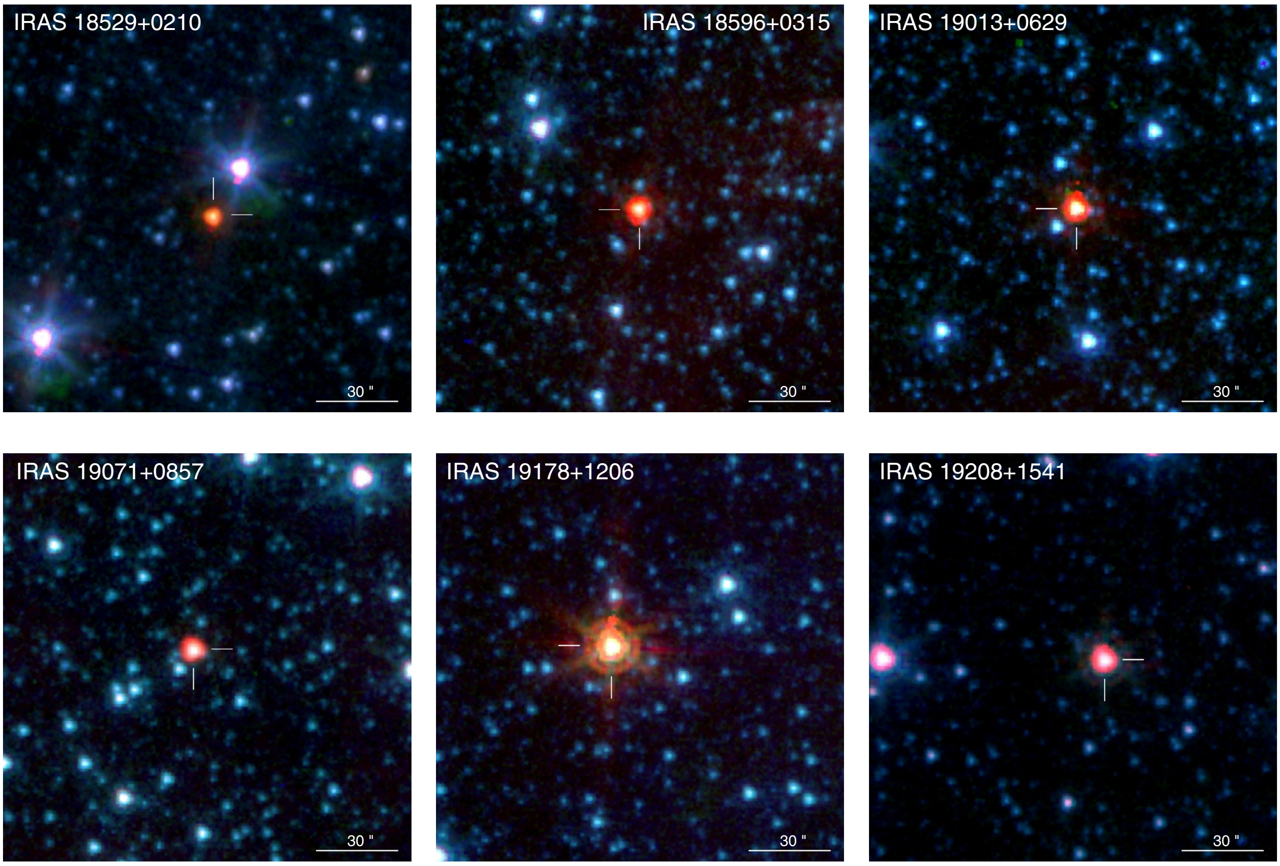

Fig. 3. continued.

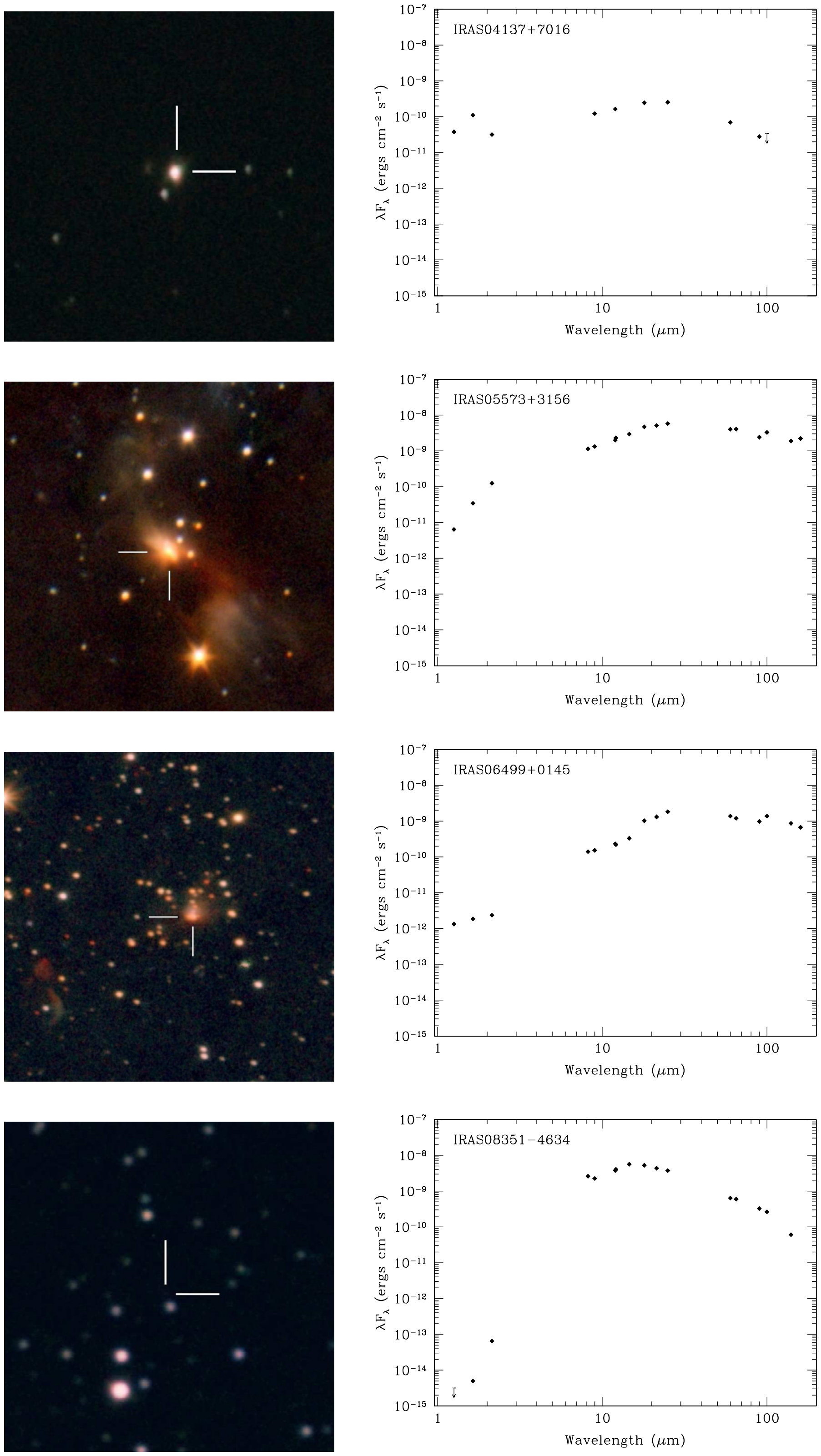

Fig. 4. (*Left*) TNG and NTT *J* (blue), *H* (green), and K_S (red) composite pictures and (*right*) IR spectral energy distributions (SEDs) of the IRAS post-AGB star and PN candidates. In the pictures, north is up, east to the left. The field of view is 1′, but for IRAS 05573+3156 and IRAS 06499+0145 which is 1.′5. The SEDs are built using our *JHK* photometric measurements and data extracted from the *Spitzer* GLIMPSE, MSX, AKARI, and IRAS catalogs. The arrows at *J*, *H*, *K*, or 100 μm represent flux upper limits (in the case of 100 μm, IRAS quality-factor, FQUAL, equals to 1).

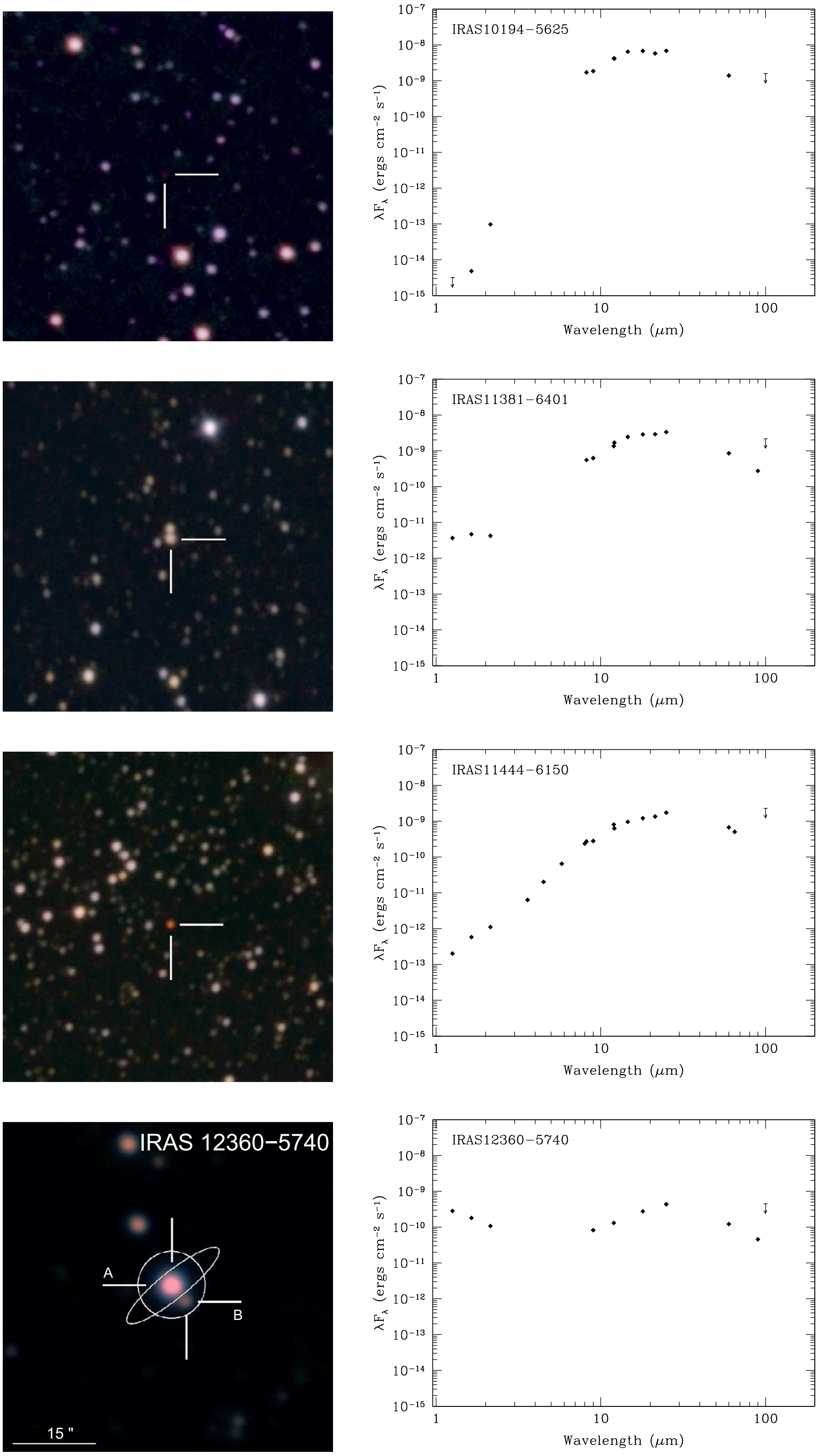

Fig. 4. continued.

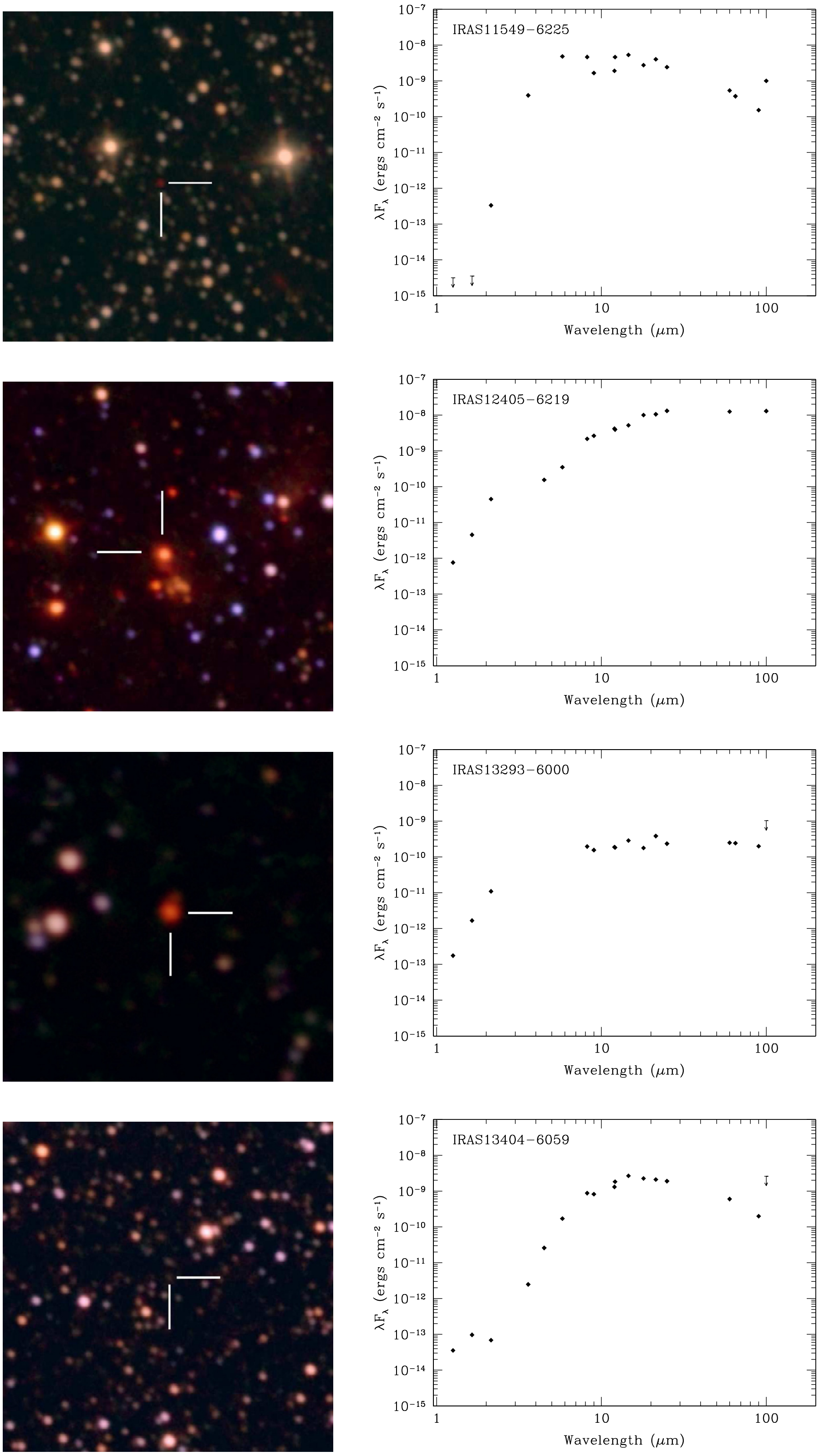

Fig. 4. continued.

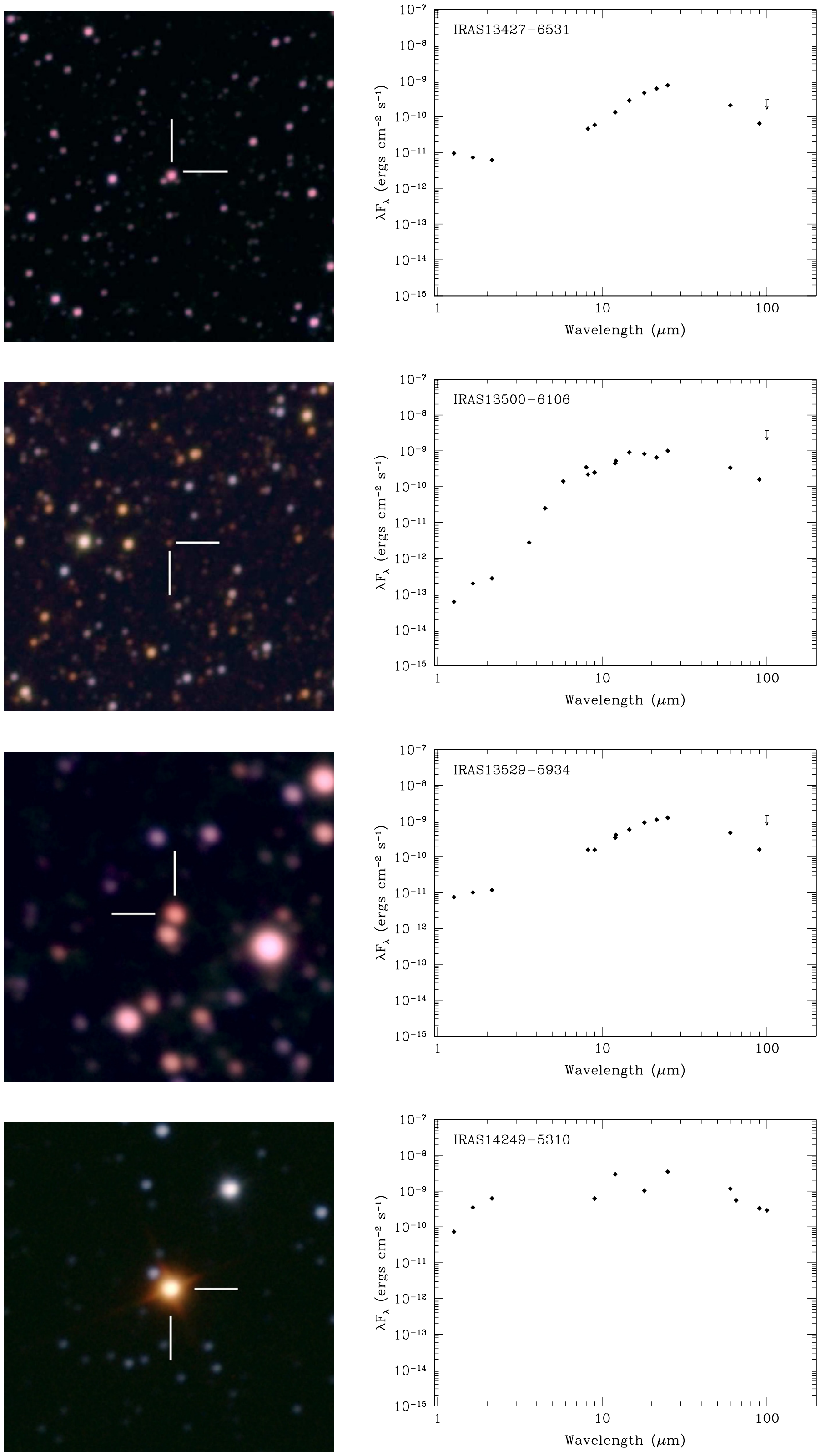

Fig. 4. continued.

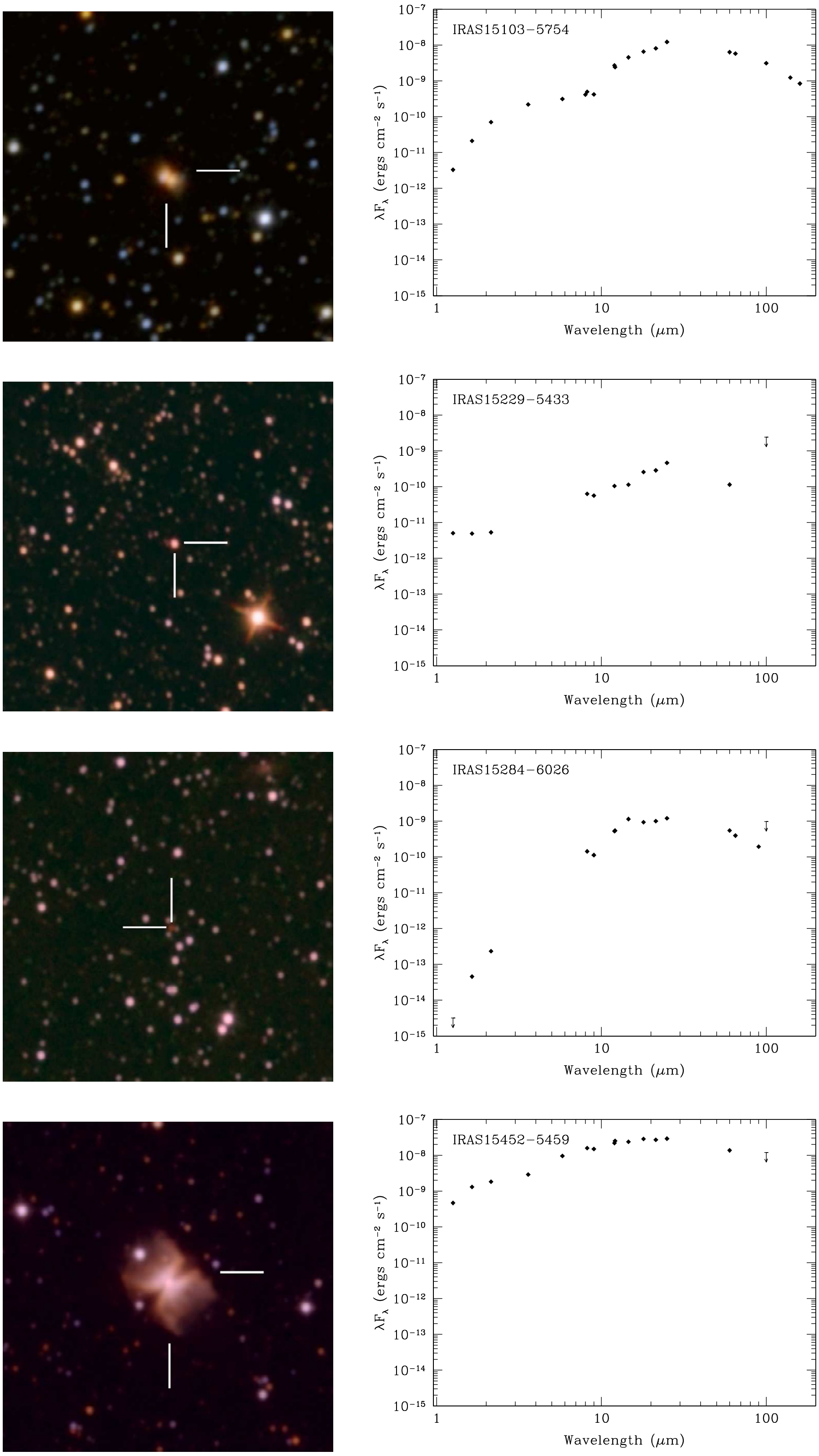

Fig. 4. continued.

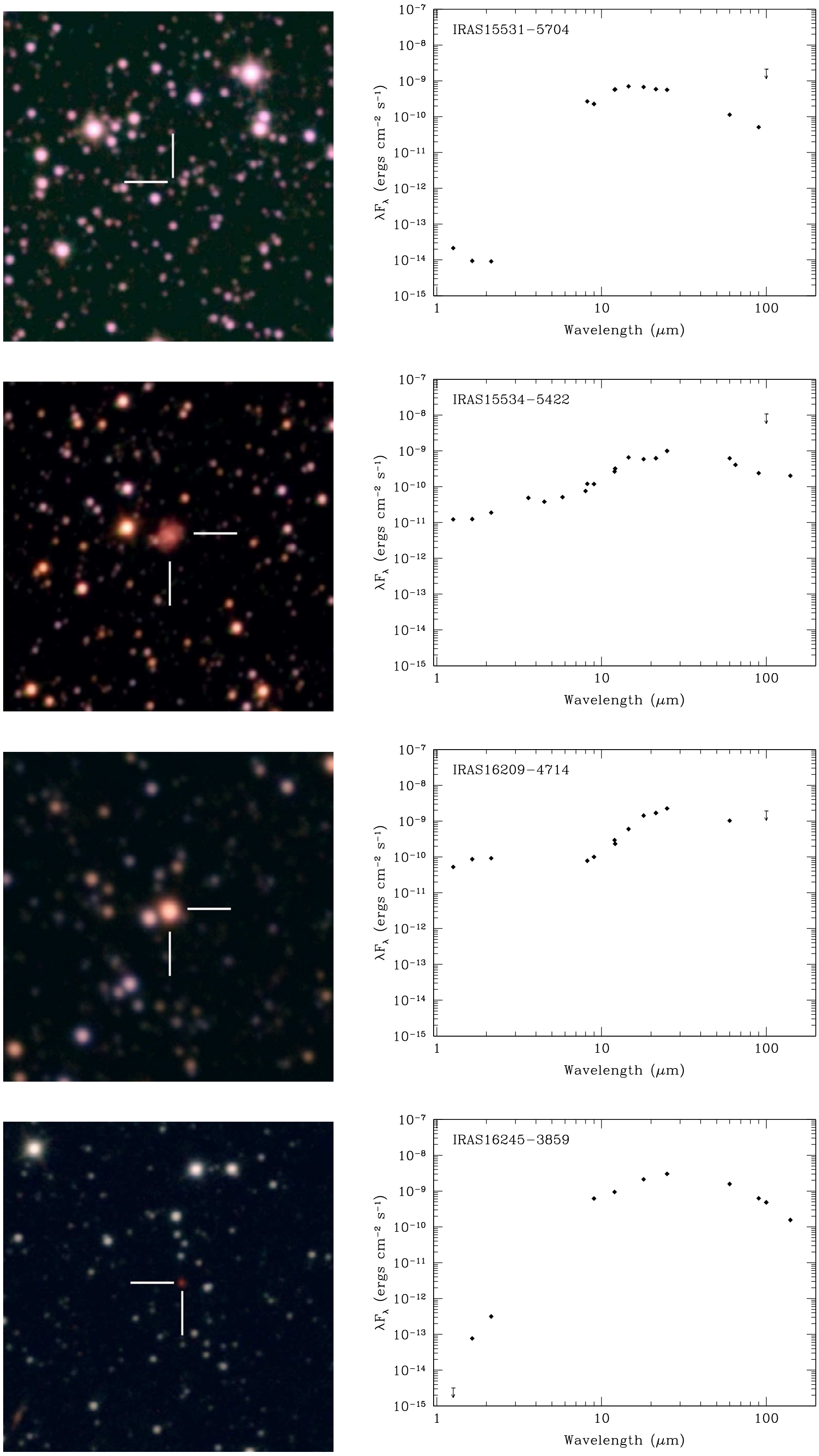

Fig. 4. continued.

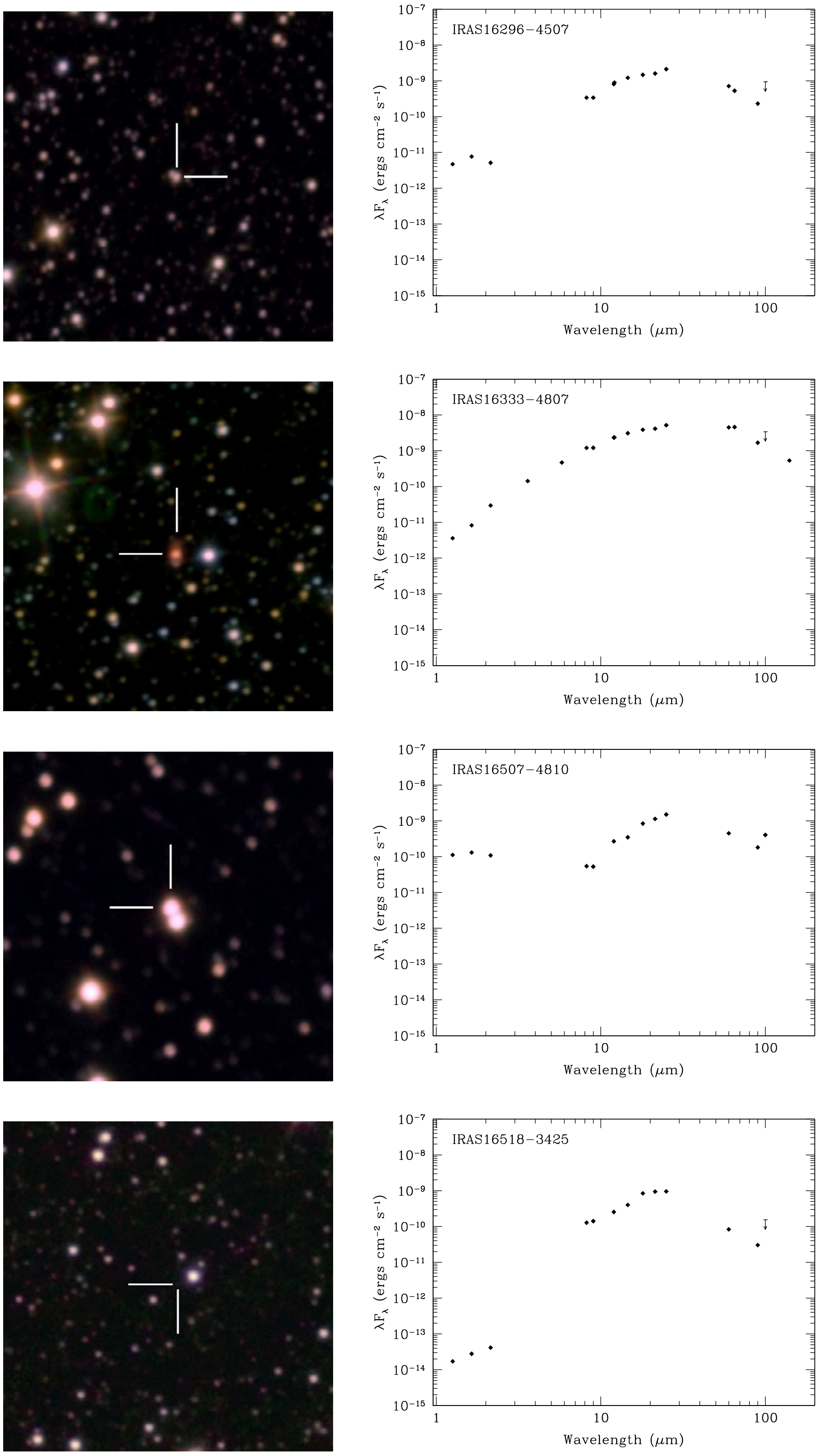

Fig. 4. continued.

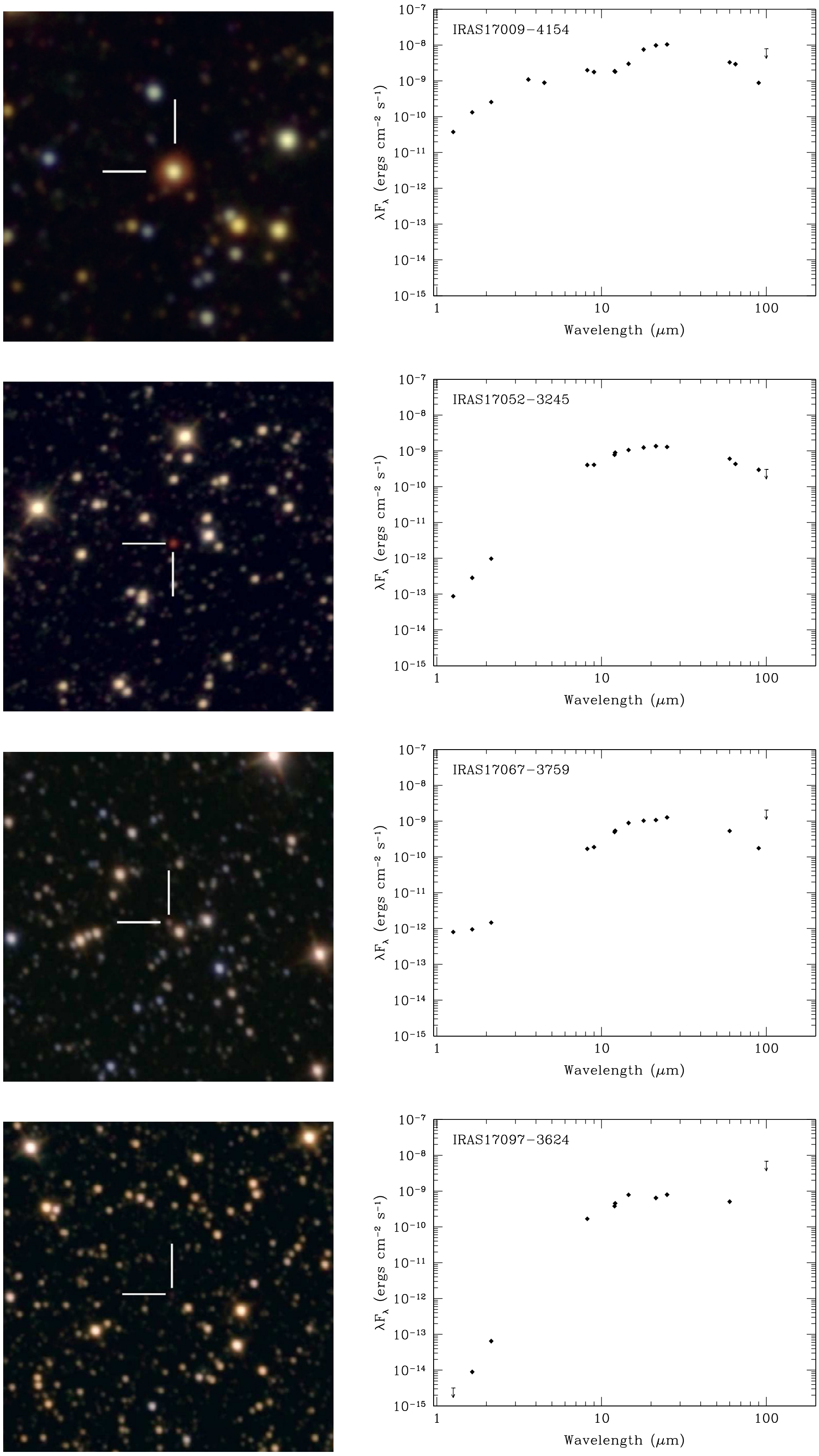

Fig. 4. continued.

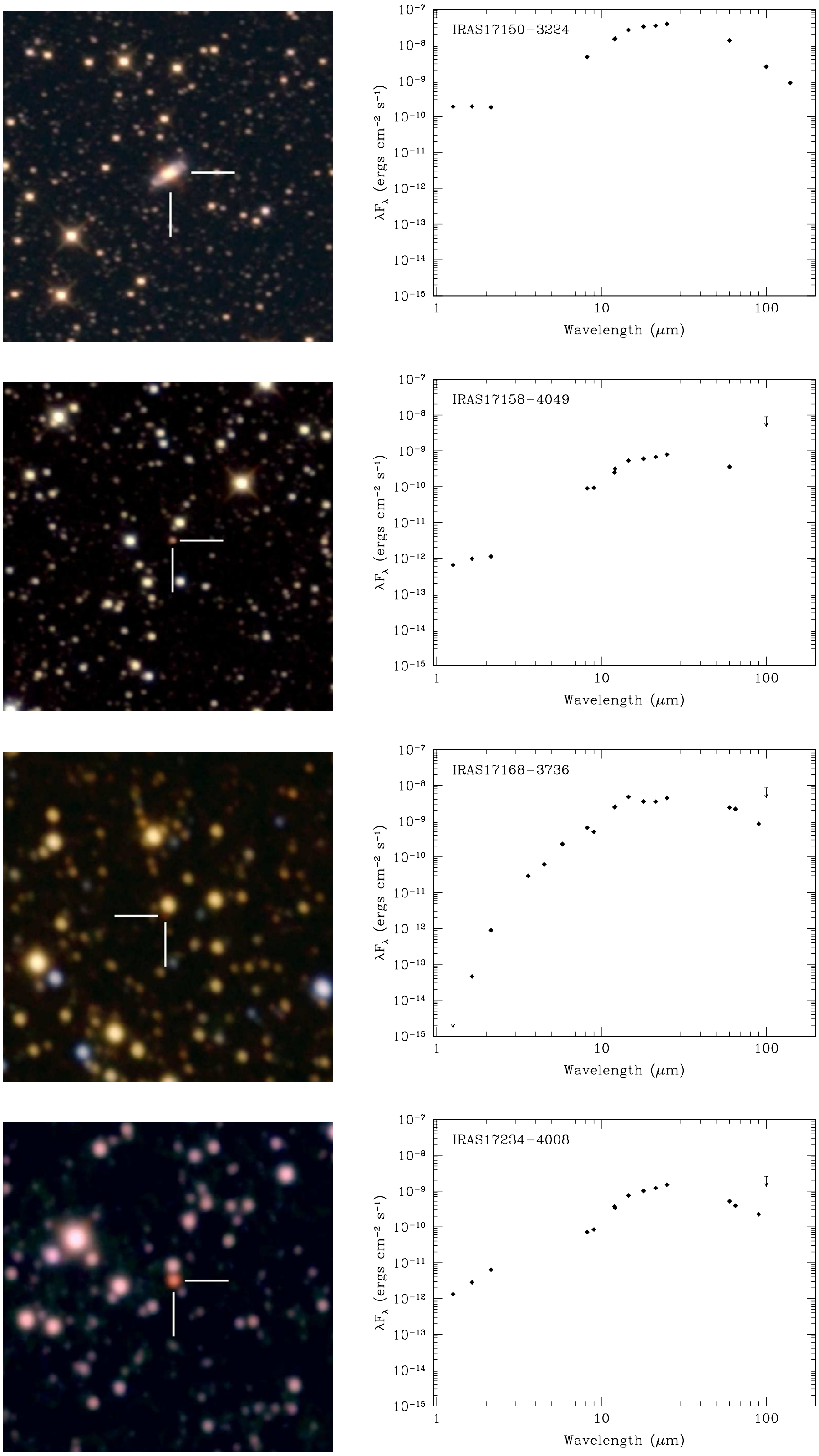

Fig. 4. continued.

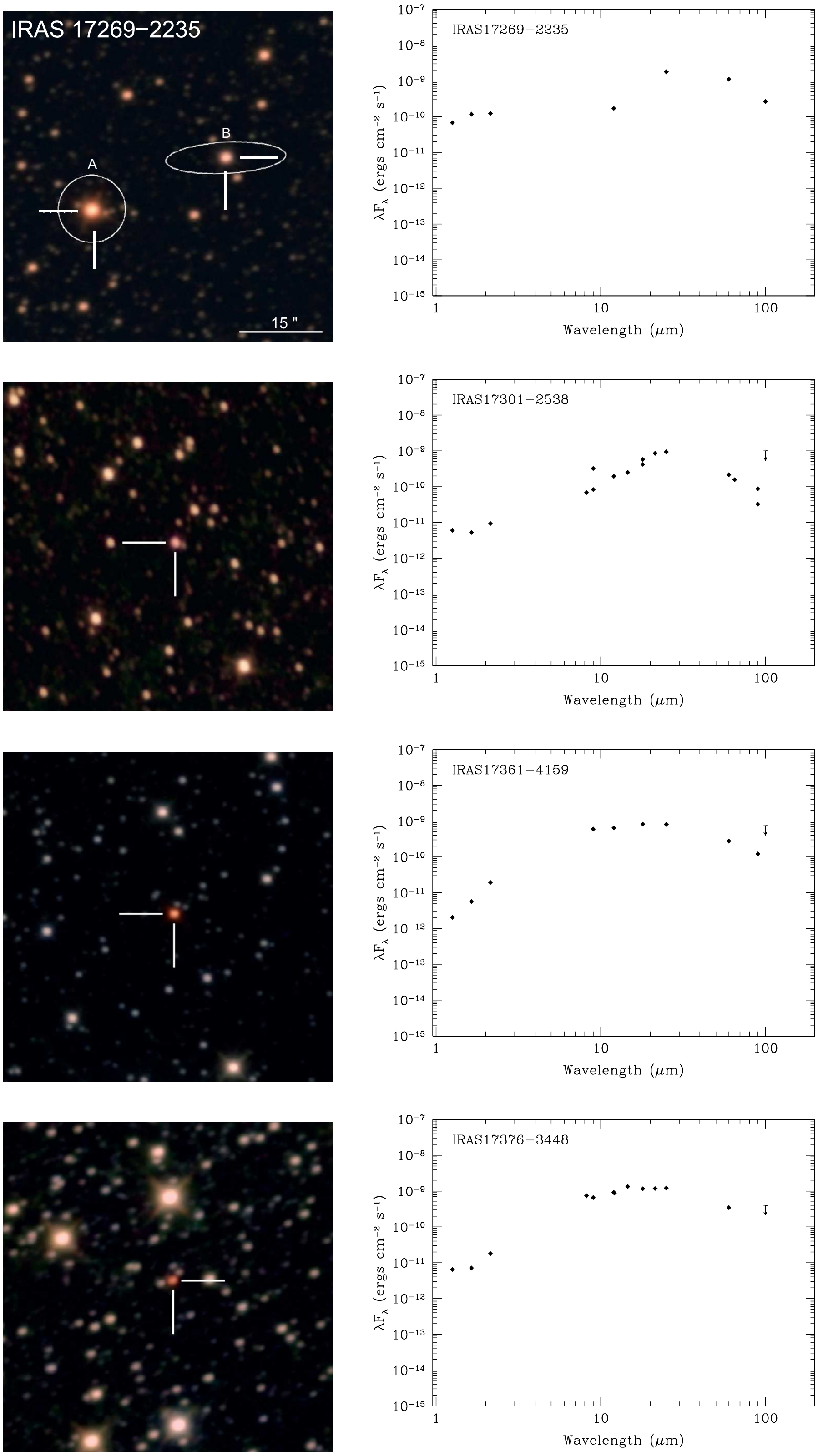

Fig. 4. continued.

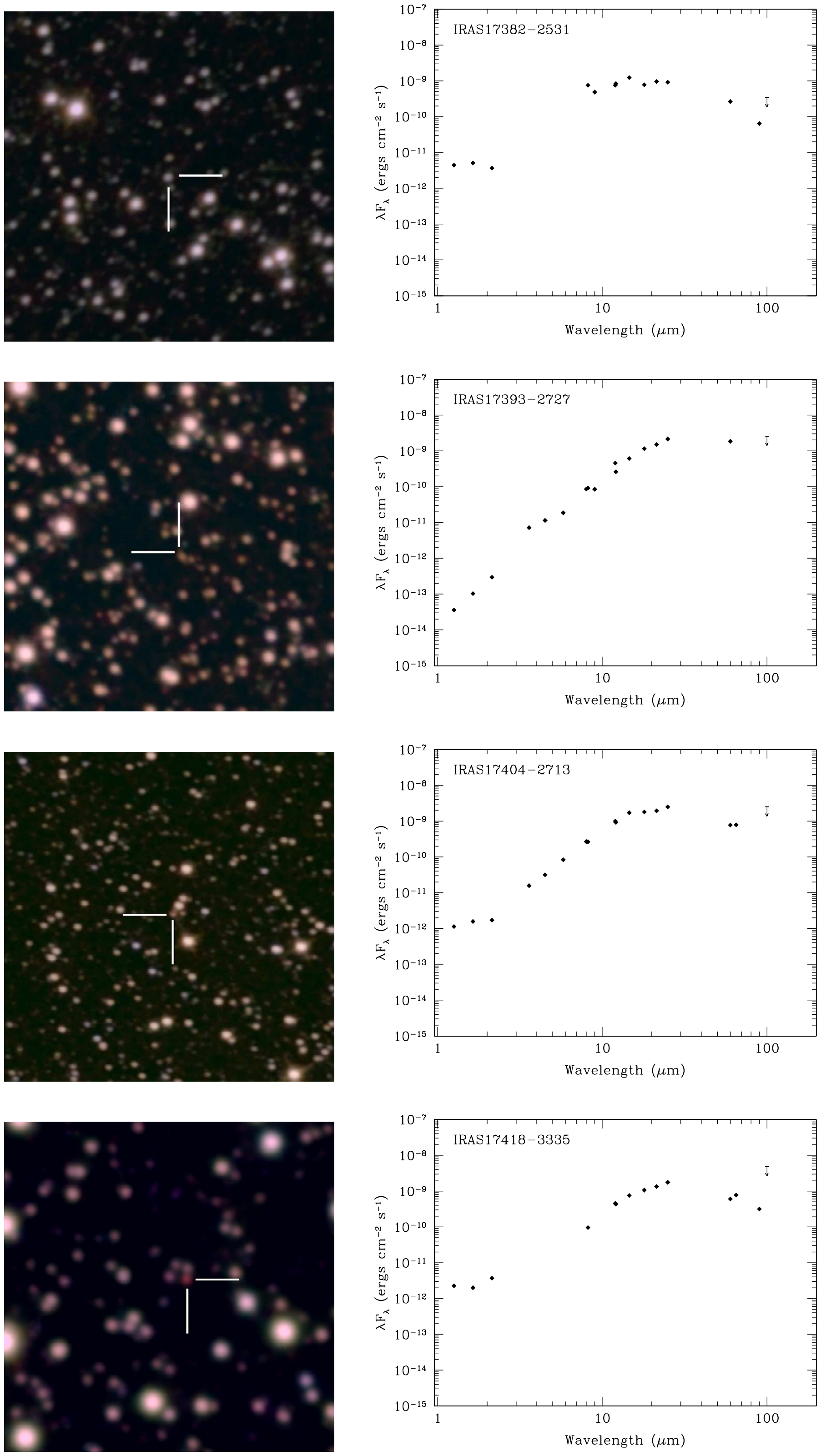

Fig. 4. continued.

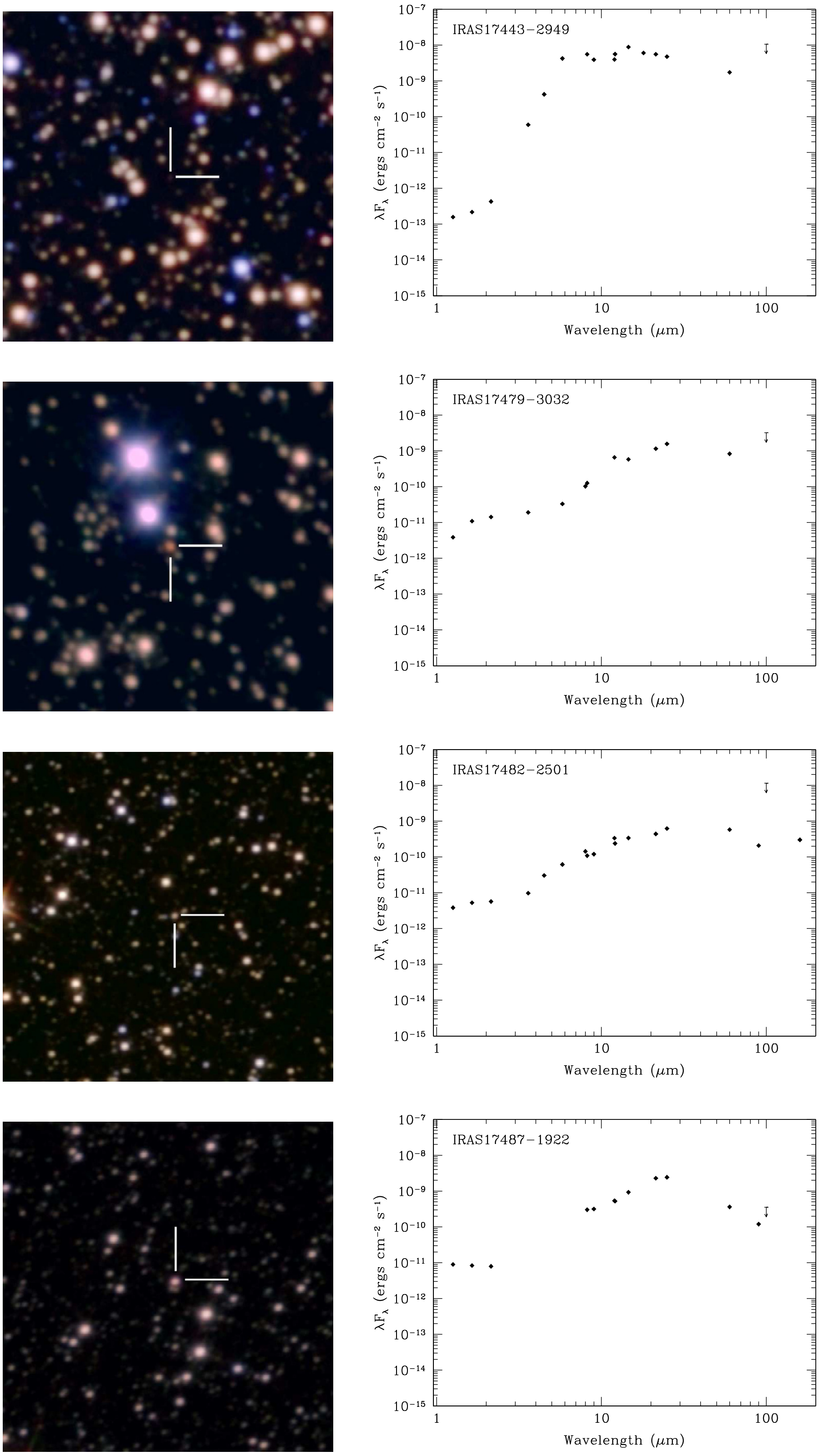

Fig. 4. continued.

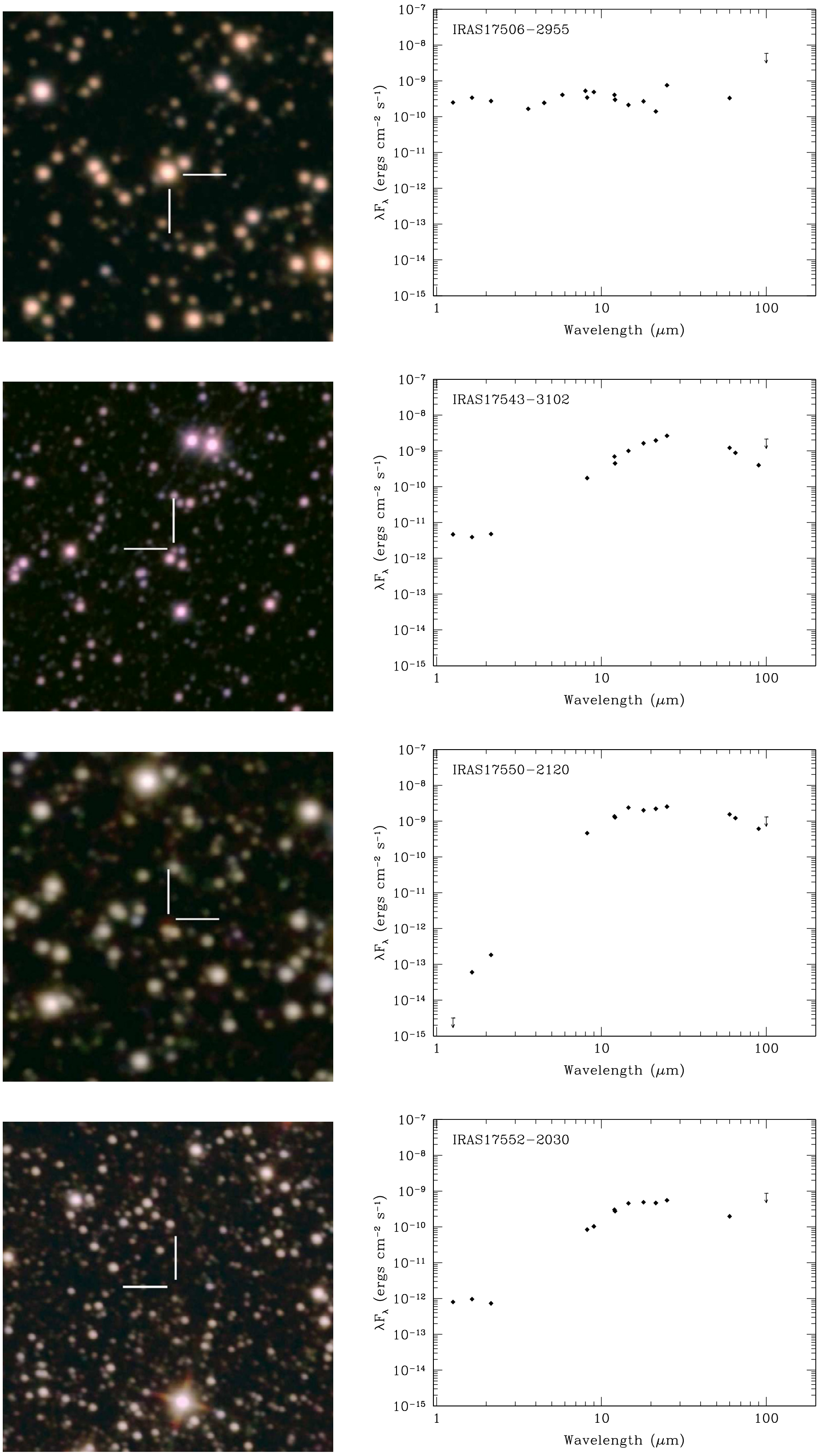

Fig. 4. continued.

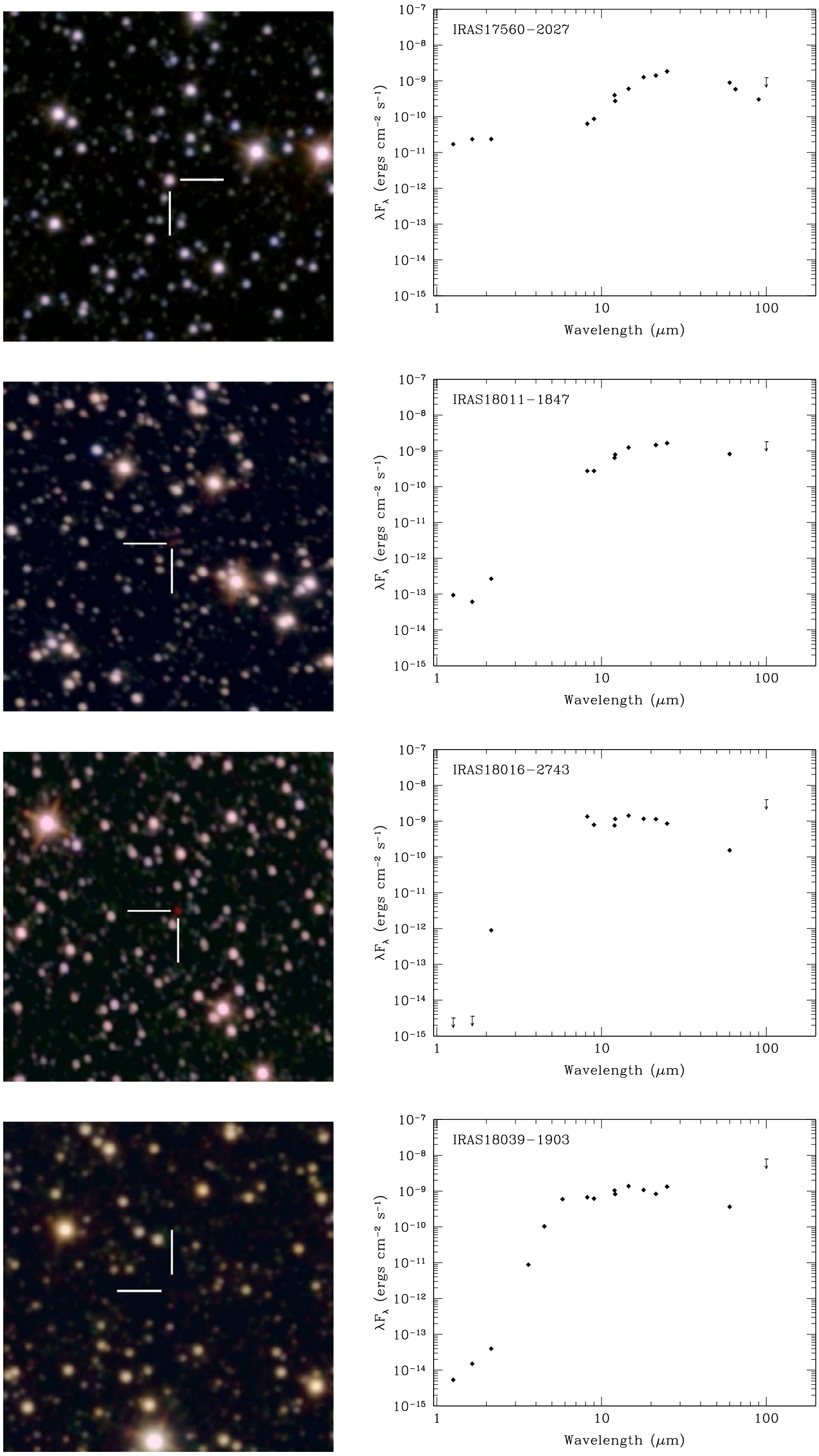

Fig. 4. continued.

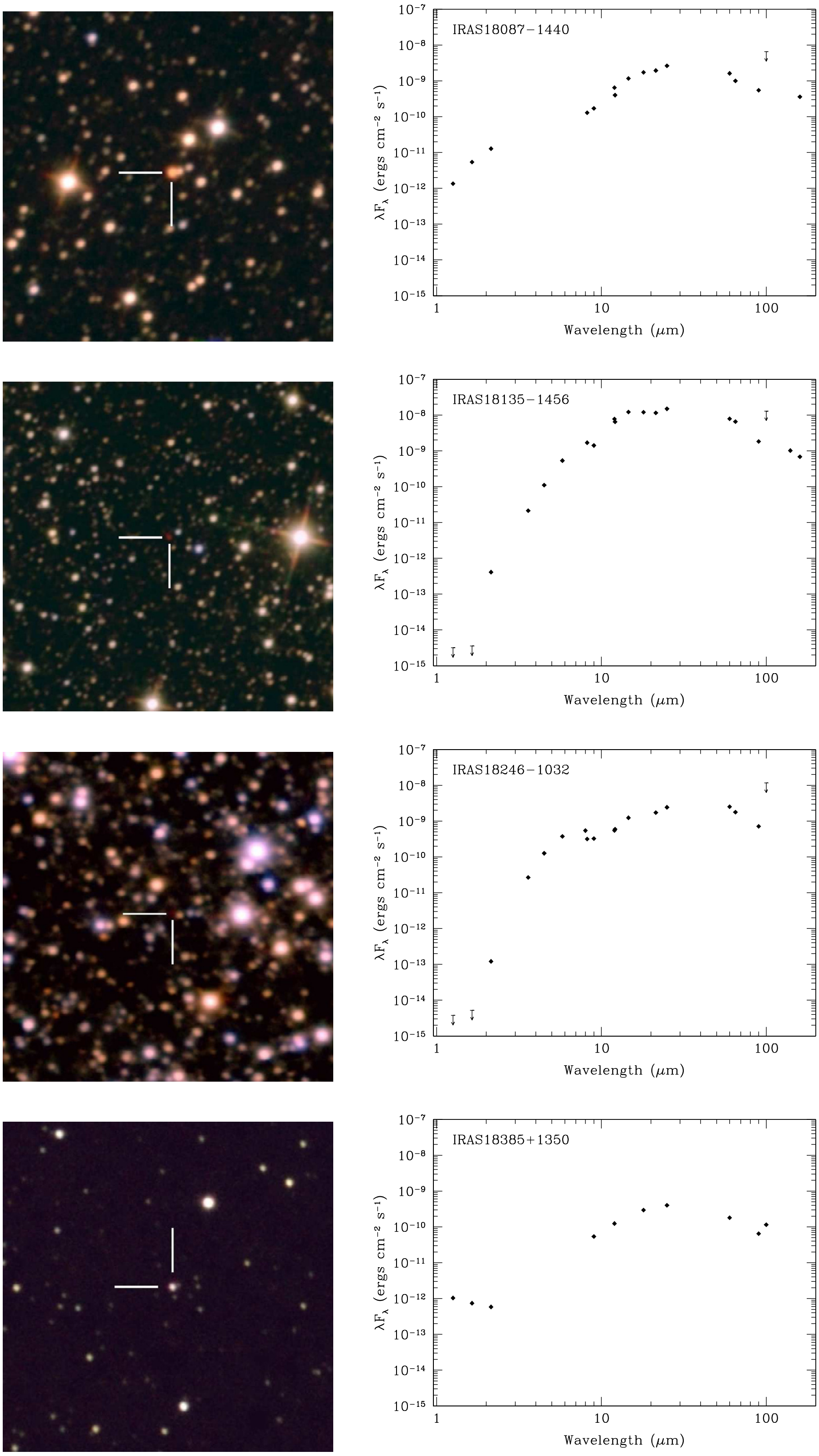

Fig. 4. continued.

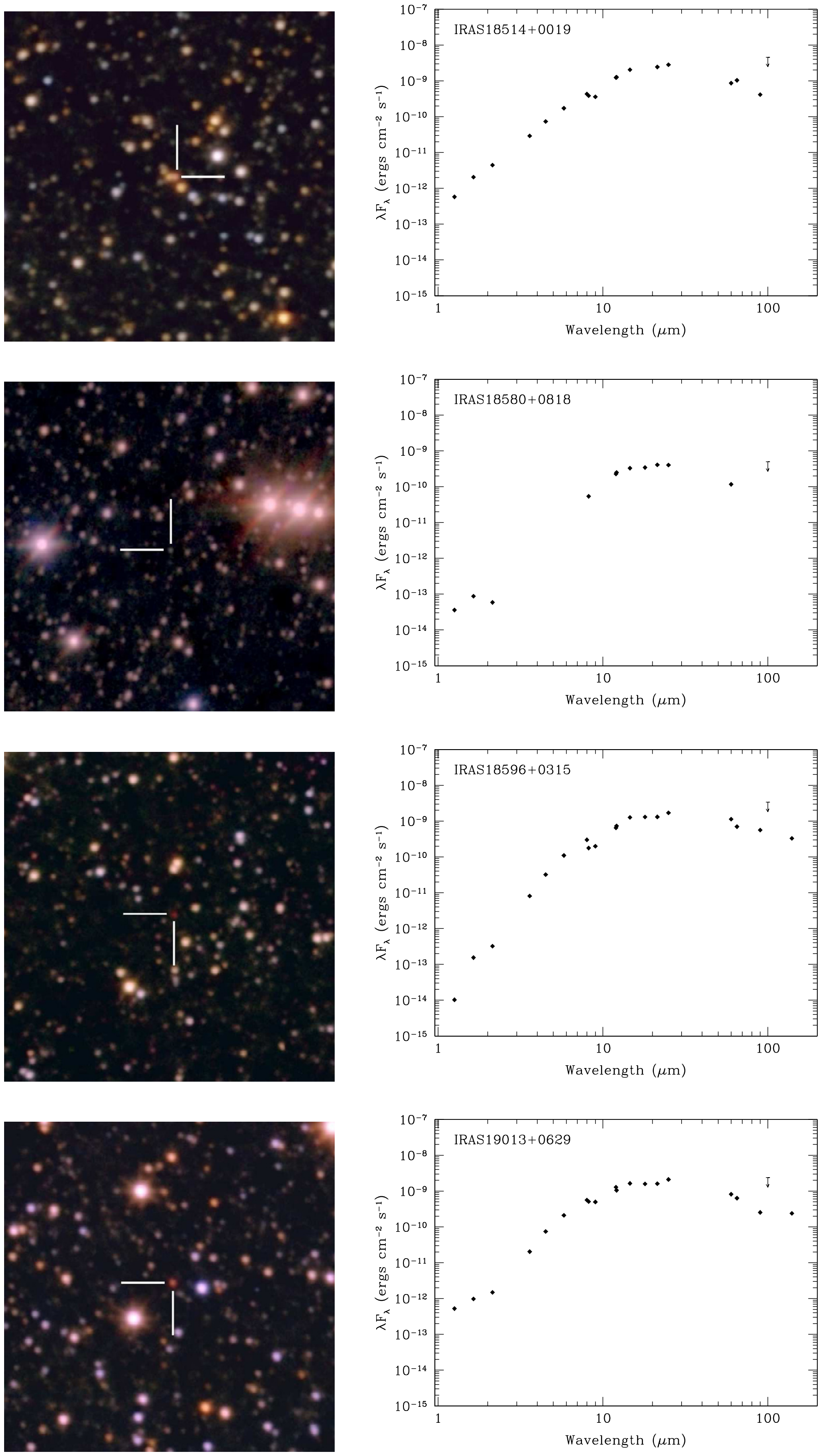

Fig. 4. continued.

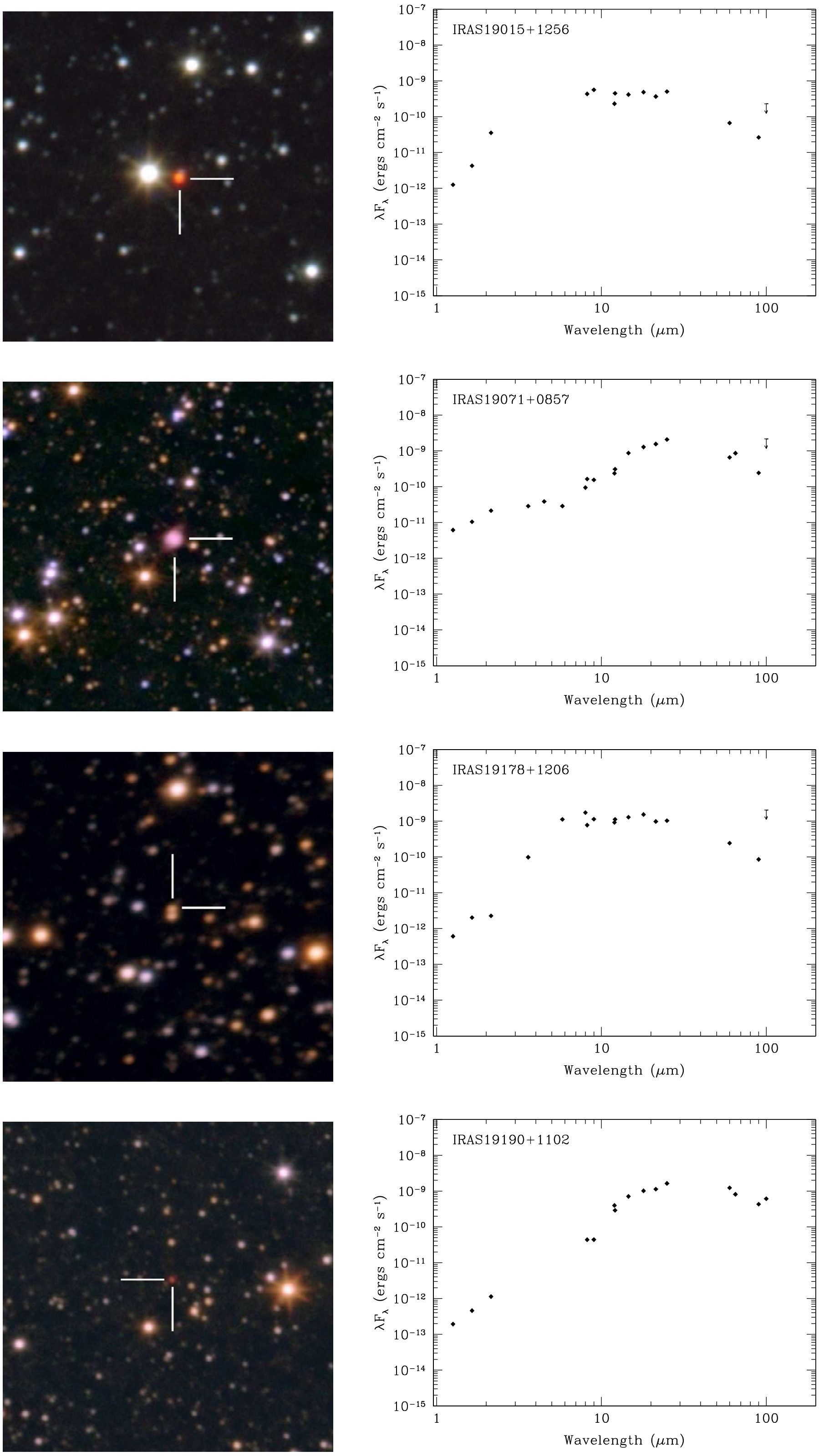

Fig. 4. continued.

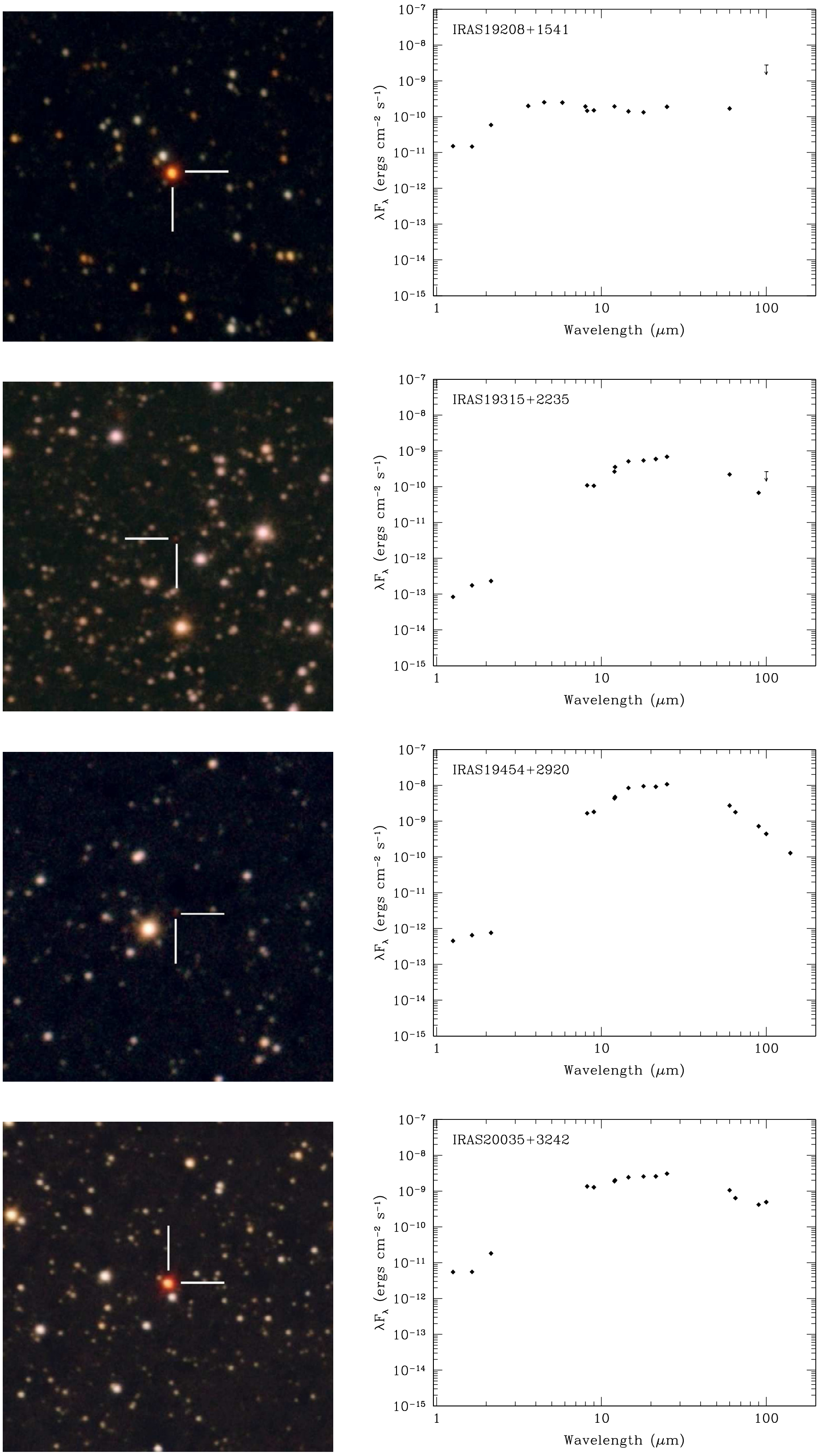

Fig. 4. continued.

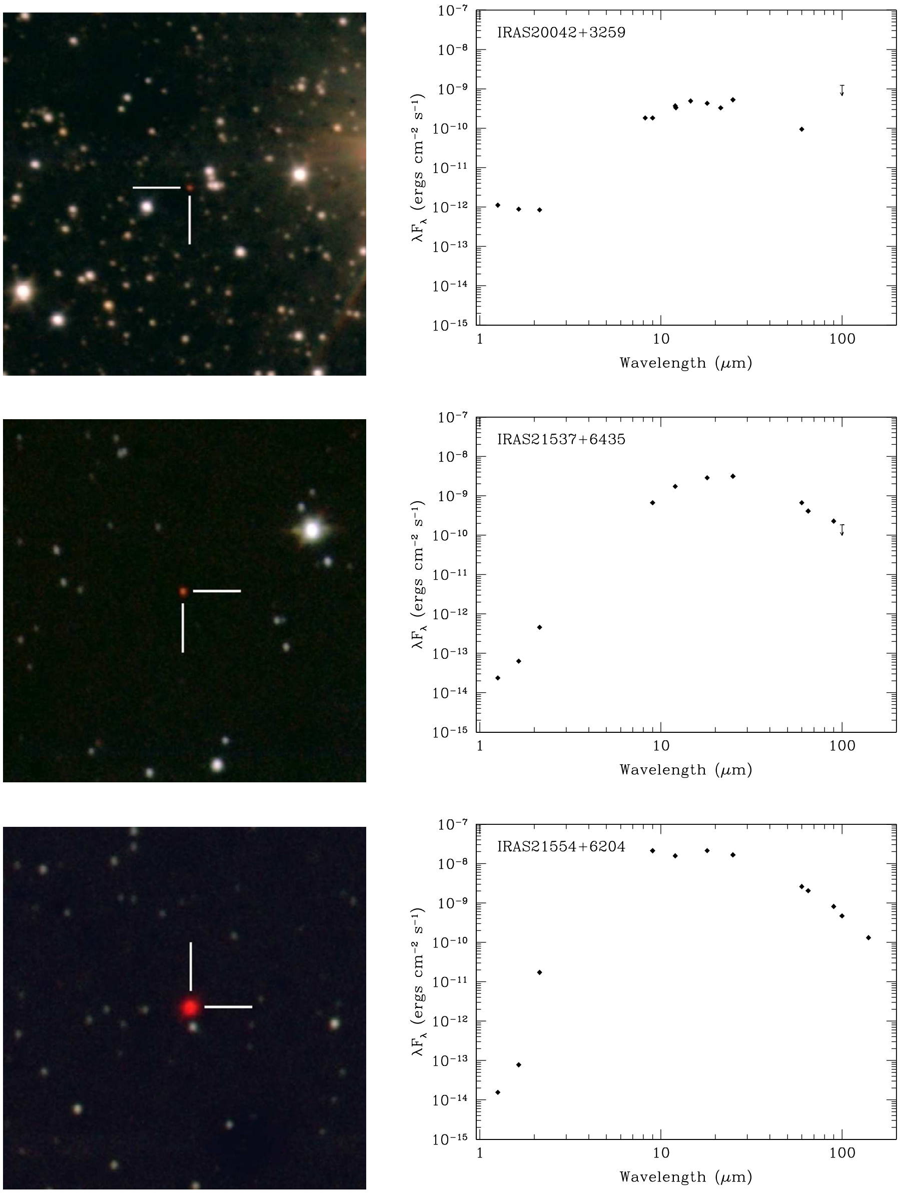

Fig. 4. continued.

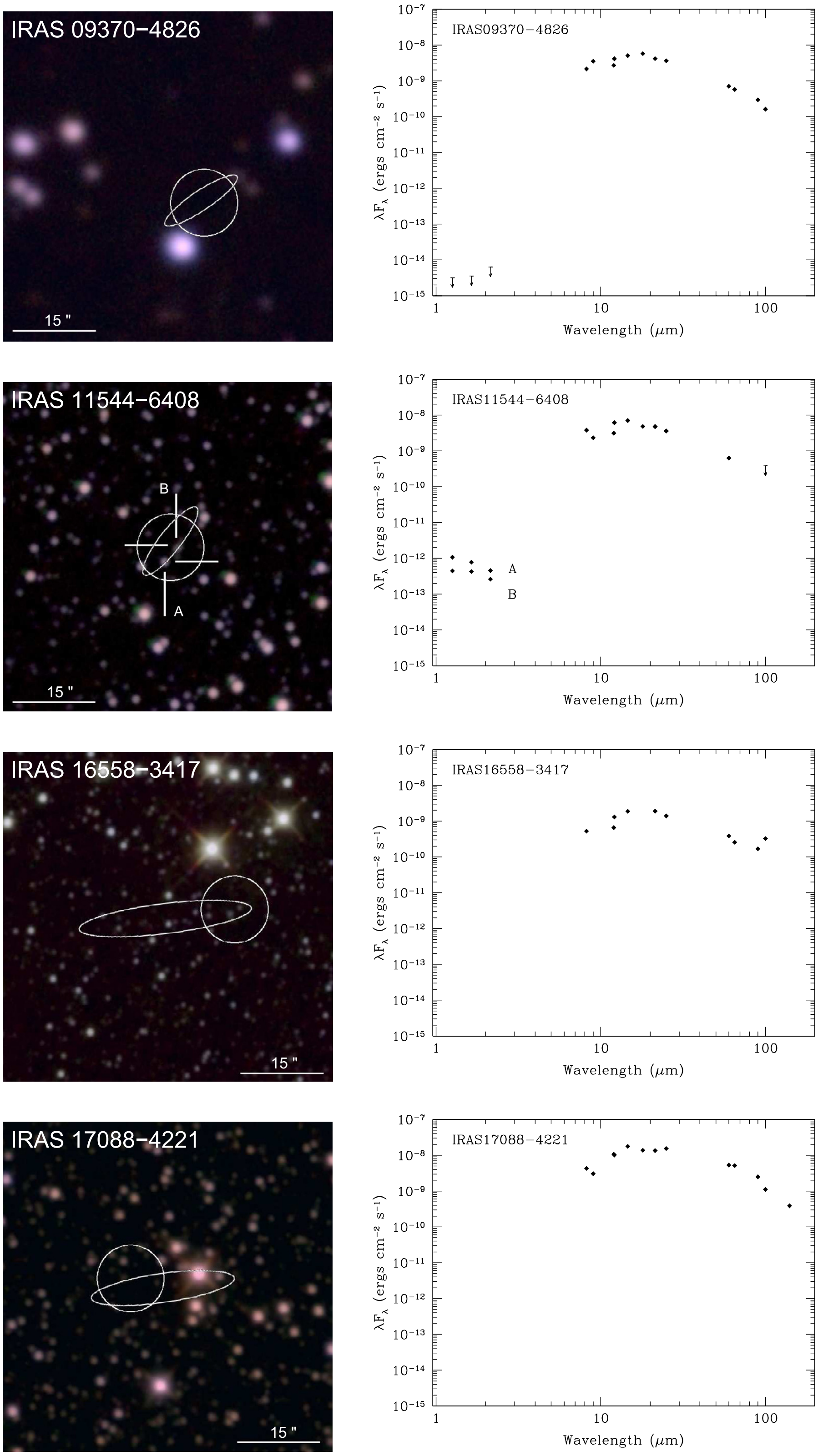

Fig. 5. Same as Fig. 4, but for IRAS post-AGB star and PN candidates whose near-IR counterparts are not detected or unambiguously detected. When two near-IR counterparts are possible, these are overlaid as "A" and "B" on the image and the *JHK* photometry of both sources listed in Table 7 are shown in their corresponding SED. When no unambiguous near-IR counterpart can be selected, the respective ellipse and circle errors of the IRAS and MSX coordinates are overlaid on the image. As for IRAS 18529+0210, the accurate location of the *Spitzer* counterpart is marked on the figure and the *JHK* photometry upper limits are shown on its SED. The field of view of the images is 1′. North is top, east is left.

)

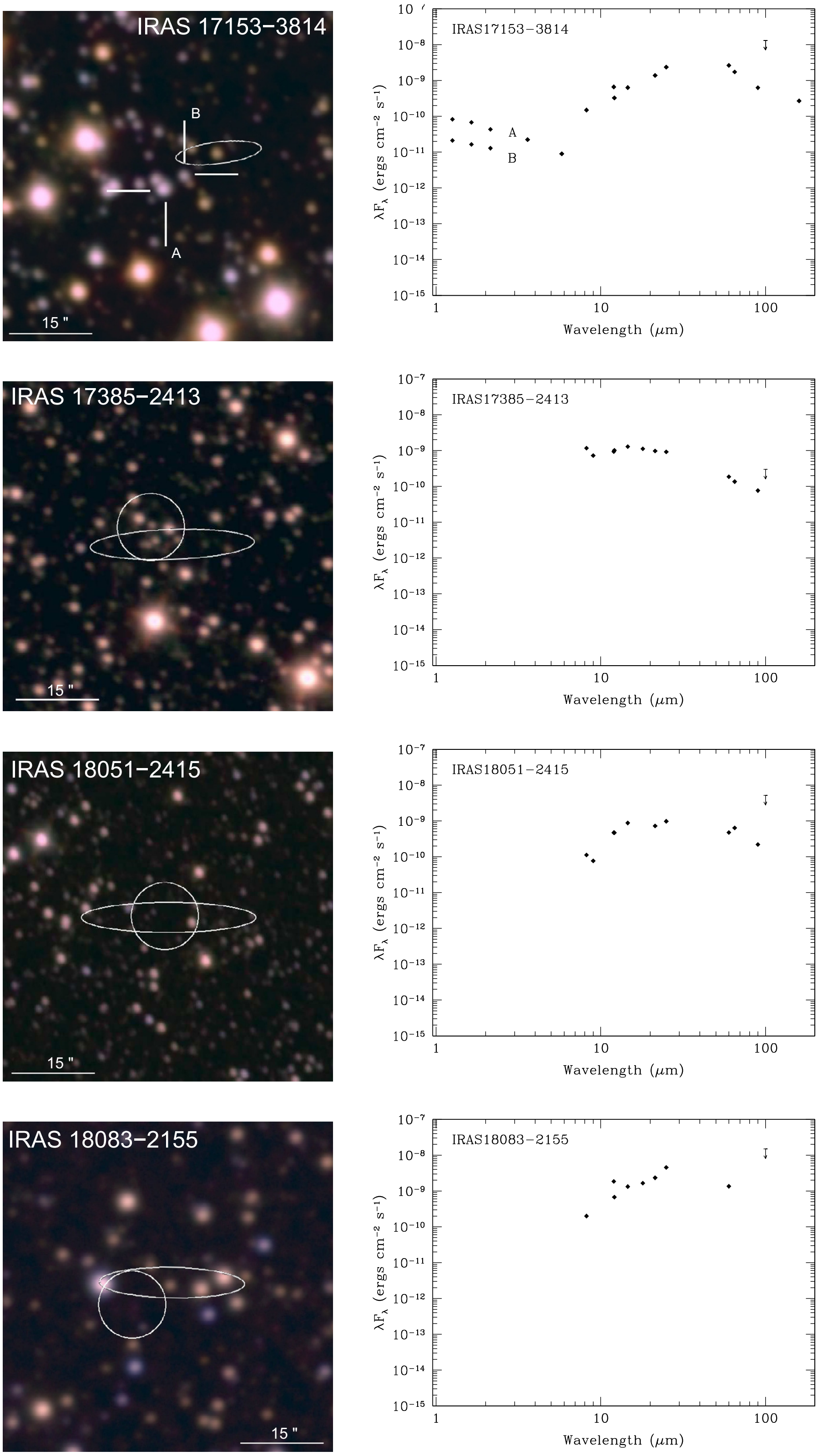

Fig. 5. continued.

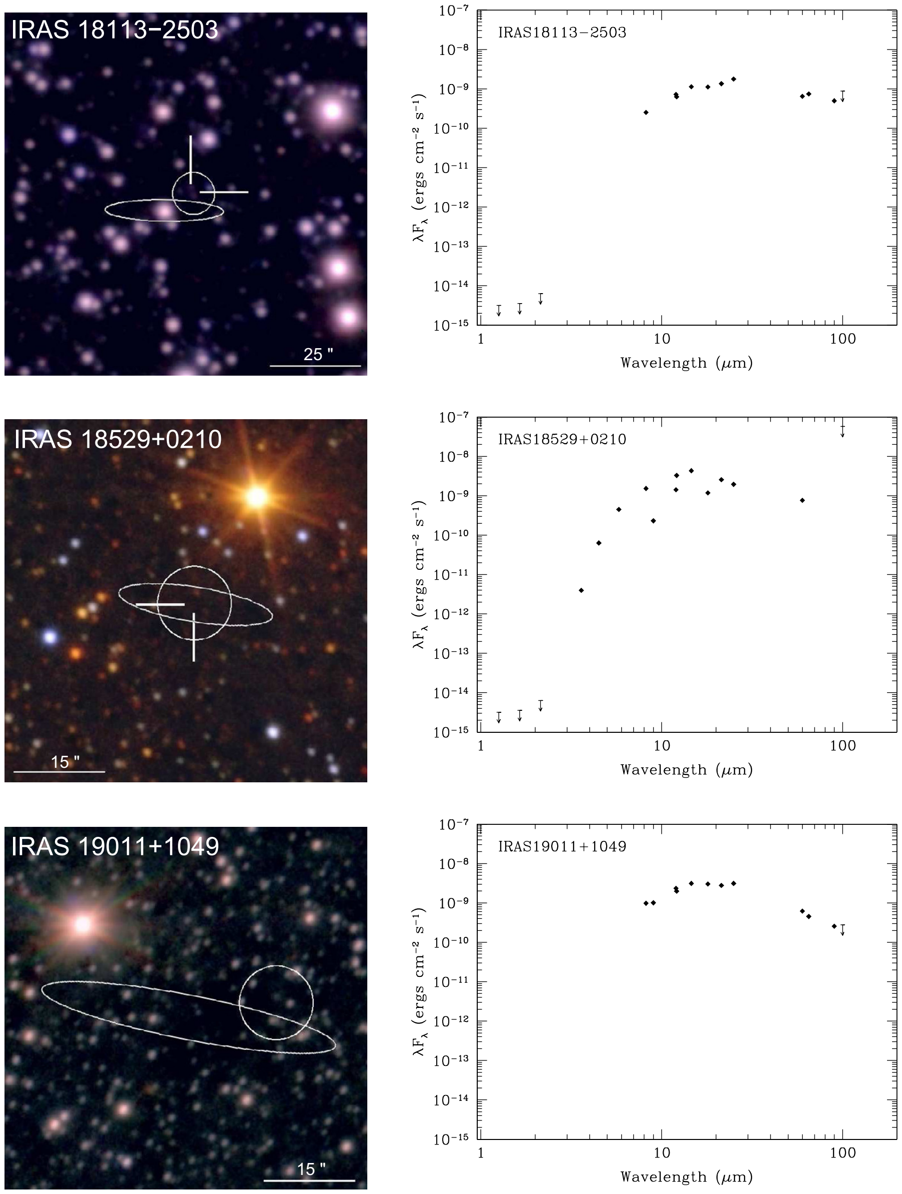

Fig. 5. continued.